CHEMISTRY OF MATERIALS

pubs.acs.org/cm

Article

Origin of Aging of a P2-$Na_xMn_{3/4}Ni_{1/4}O_2$ Cathode Active Material for Sodium-Ion Batteries

Lukas Fridolin Pfeiffer,* Yueliang Li, Manuel Mundszinger, Jonas Geisler, Claudia Pfeifer, Daria Mikhailova, Ahmad Omar, Volodymyr Baran, Johannes Biskupek, Ute Kaiser, Philipp Adelhelm, Margret Wohlfahrt-Mehrens, Stefano Passerini, and Peter Axmann*

Cite This: *Chem. Mater.* 2023, 35, 8065−8080

Read Online

ACCESS | Metrics & More | Article Recommendations | Supporting Information

ABSTRACT: Sodium-ion batteries (SIB) are currently being developed and commercialized as a promising new technology for cost-effective and powerful electrical energy storage. In this study, we investigate the origin of capacity fading in P2-type layered sodium cathode materials for SIBs using a micron-sized single-crystalline P2-$Na_xMn_{3/4}Ni_{1/4}O_2$ model cathode active material. Using various electrochemical techniques, we identify the following aging effects upon cycling: (i) a state of charge (SOC)-independent increase in polarization, (ii) a SOC-dependent increase in polarization at high voltage, and (iii) a loss of active material due to electronic disconnection after prolonged cycling. With high-resolution transmission electron microscopy (HRTEM) and energy-dispersive X-ray (EDX) spectroscopy, we identify surface densification, resulting in 5−10 nm thick surface layers on cycled cathode active materials as the origin for SOC-independent increase of polarization. The corresponding oxygen loss is in accordance with gas evolution in differential electrochemical mass spectrometry (DEMS) measurements. Furthermore, with scanning electron microscopy (SEM) electrode cross sections, we identify (partly) reversible cracking at a high SOC as the cause for increased polarization depending on SOC. Operando X-ray diffraction (XRD) identifies significant anisotropic volume change, which suggests mechanical stress as the cause for cracking at a high SOC and loss of active material after prolonged cycling. We believe that the herein provided understanding on the aging of this highly attractive class of cathode active materials for SIBs will enable the development of future powerful and stable layered oxide cathode materials for SIBs.

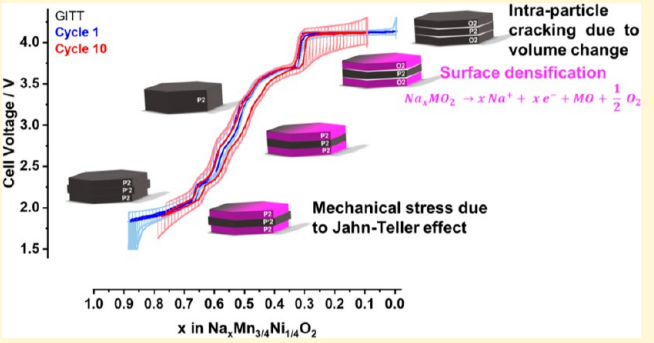

INTRODUCTION

Electrical energy generation from renewables and storage thereof lies at the heart of the worldwide transition toward climate neutrality. Due to their high efficiency and high energy density, lithium-ion batteries (LIBs) play a key role in mobile and stationary energy storage.[1−3] With the worldwide increasing demand for LIBs, possible supply limitations and resulting price increases for critical raw materials, such as lithium, cobalt, nickel, and graphite, could potentially slow down this essential transition.[4−6]

Sodium-ion batteries (SIB) utilize the same working principle as LIBs[7] but are designed to operate without (or with minimal) critical raw materials.[8,9] Therefore, SIBs are currently developed and industrialized as a new, sustainable technology to complement current LIBs.[8,10,11] In a typical rocking-chair type SIB, sodium ions replace lithium ions as ionic charge carriers. On the anode side, hard carbon—often derived from sustainable sources such as biowaste—replaces graphite as an active material.[12−14] On the cathode side, sodium-containing intercalation compounds replace lithium cobalt manganese nickelates (NCM) or lithium iron phosphate (LFP).[8,15] Cheap and lightweight aluminum foils can be used as a current collector for both the anode and cathode, replacing copper on the anode side of LIBs.[15−17] Furthermore, SIBs may offer desirable advantages against LIBs in terms of low-temperature performance,[10] 0 V storage and transport,[18] as well as possibly enhanced battery safety.[19,20] Collectively, these measures result in significantly reduced raw material costs and potentially more sustainable batteries.[21−24] Additionally, sodium-ion batteries can be produced based on the same production processes and manufacturing lines as current lithium-ion batteries (drop-in technology), which minimizes necessary investments and potentially accelerates industrializa-

Received: June 15, 2023
Revised: August 22, 2023
Published: September 25, 2023

tion, making SIBs a promising complementary technology to LIBs.[15]

It must be noted that current sodium-ion batteries still come with a slight cost disadvantage based on the amount of stored energy ($/kWh).[17,21,25] However, limited availability and projected price increase for lithium and other critical raw materials or the development of materials with higher energy density for SIBs might reverse this trend in the near future.[6,21]

The cathode active material remains one of the main bottlenecks toward cost-effective, powerful, and sustainable SIBs. Layered sodium transition metal oxides are amongst the most promising cathode active materials due to their high density, suitable energy, and power output and the possibility to manufacture these materials in similar ways as current NCM materials for LIBs.[8,9,26−28] These compounds offer a wide structural variety and can be synthesized as O3, P3, and P2 types, following Delmas' notation for alkali metal layered oxides.[29,30] Among these, P2-type materials are reported to be beneficial in terms of structural stability during electrochemical (de)sodiation and fast solid-state diffusion (e.g., rate capability).[31]

P2-type sodium manganese nickel layered oxides offer a good mix of high energy density, power capability, and sustainability. One of the most prominent compositions of this material class is P2-$Na_{2/3}Ni_{1/3}Mn_{2/3}O_2$,[8] which was first reported by Dahn and co-workers.[32−34] During electrochemical (de)sodiation at room temperature, P2-$Na_xNi_{1/3}Mn_{2/3}O_2$ maintains the P2 structure over a wide range of stoichiometry ($x \geq 1/3$), following solid solution-like behavior.[33] At sodium stoichiometries $x < 1/3$, a two-phase reaction with the respective endmembers P2-$Na_{1/3}Ni_{1/3}Mn_{2/3}O_2$ and O2-$Na_0Ni_{1/3}Mn_{2/3}O_2$ takes place.[33] The potential profile of this material typically shows distinct voltage jumps at sodium stoichiometries of $x = 2/3$, 1/2, and 1/3, which are associated with Na^+/vacancy orderings.[33,35] In sodium cells, this material is capable of delivering specific discharge capacities of approximately 160 mAh g^{-1} at an average potential of approximately 3.6 V when cycled between 2.0−4.5 V vs Na/Na^+.[33,36,37] When the potential window is expanded to 1.5−4.5 V, discharge capacities of ≥ 220 mAh g^{-1} at a mean potential of approximately 3.1 V are reached.[38,39] When the nickel content is further decreased to P2-$Na_xMn_{3/4}Ni_{1/4}O_2$, similar electrochemical performance can be achieved.[40−42]

At high potentials (≥4 V), charge is either compensated by oxygen redox, following a reductive coupling mechanism[38,43,44] or by $Ni^{3+/4+}$ cationic redox.[33,37] At medium potentials (approximately 2.5−4 V), charge is compensated by $Ni^{2+/3+}$ redox couple.[38] At low potentials (approximately <2.5 V), $Mn^{3+/4+}$ redox couple is active.[38]

So far, the main drawback of these materials is their low cycling stability. Typically, for P2-type $Na_xNi_yMn_{1-y}O_2$, the capacity fades quickly during the first ten to twenty cycles when the upper cutoff exceeds 4 V vs Na/Na^+.[45] In the literature, the pronounced capacity fade has been assigned to exfoliation,[46,47] side reactions with the electrolyte,[38] partial irreversibility of the P2/O2 phase transition,[36] surface densification,[44] or oxygen redox.[43] Yet, despite considerable efforts, the underlying aging mechanism for this highly promising material class remains elusive.

In this work, we have synthesized micron-sized single-crystal P2-$Na_xMn_{3/4}Ni_{1/4}O_2$ as a model material to investigate the origin of the capacity fade of this promising class of cathode active materials for sodium-ion batteries. The chemical, physical, and electrochemical properties of the obtained material are thoroughly characterized. By combining several characterization techniques, we provide evidence for two aging mechanisms, namely, surface densification and intracrystallite cracking. Based on these results, we postulate and discuss an aging mechanism for this material class.

EXPERIMENTAL SECTION

Material Synthesis. We have synthesized micron-sized single-crystal P2-$Na_xMn_{3/4}Ni_{1/4}O_2$ in a multistep process starting from a spherical $Mn_{3/4}Ni_{1/4}(OH)_2$ precursor, which was obtained by coprecipitation in a continuously stirred tank reactor as described elsewhere.[42] These dense spherical particles were disintegrated by ball milling. The resulting powder was mixed with Na_2CO_3 (Sigma-Aldrich) and NaCl (Sigma-Aldrich) in molar ratios of Na_2CO_3/M = 0.44 and NaCl/M = 0.55, respectively, and then calcined for 24 h in air at 1000 °C in a batch furnace (Nabertherm). The obtained powder was washed with deionized water (5 mS cm^{-1}), filtered, dried, and subsequently mixed with Na_2CO_3 and Na_2SO_4 (Alfa Aesar) in molar rations of $Na_2CO_3/M \approx 0.10$ and $Na_2SO_4/M \approx 0.55$, respectively. The obtained mixture was calcined in the same batch furnace for 10 h in air at 1000 °C, subsequently washed in deionized water, filtered, dried, and ground with a mortar and pestle. Final calcination in CO_2-free synthetic air (20 vol % O_2 in Ar) for 5 h at 900 °C was performed in a box furnace (Carbolite Gero). After calcination, the obtained powder was transferred in a Büchi glass oven with minimal time at ambient conditions, dried at 200 °C under dynamic vacuum overnight, and subsequently stored in an Ar-filled glovebox (MBraun, O_2 < 0.1 ppm, H_2O < 0.1 ppm).

Material Characterization. The chemical composition was analyzed by ICP-OES (Spectro Arcos SOP) using a diluted aqua regia solution. ATR-FTIR was performed inside an Ar-filled glovebox using an Alpha spectrometer (Bruker) with an Alpha-P (Bruker) ATR unit. Powder X-ray diffraction (XRD) was performed on a D8 Advance (Bruker) in Bragg-Brentano geometry using a Cu X-ray tube and a LynxEyeXE-T detector. Rietveld refinement based on the resulting diffraction pattern was performed using TOPAS V6 software. Throughout this work, all depictions of crystal structure were generated using VESTA software.[48] The morphology of the as-prepared powder was characterized by scanning electron microscopy (SEM) with a Leo 1530 VP (Zeiss) at 5 kV acceleration voltage using an Everhart−Thornley SE detector.

Electrodes, Cells, and Electrochemistry. Slurry preparation, electrode coating, punching, and cell assembly were performed inside an Ar-filled glovebox avoiding any contact with the environment to minimize any effect due to the formation of surface impurities.[49] By dispersing the active material, conductive carbon (SuperP-Li, Imerys Graphite & Carbon), and polyvinylidene difluoride binder (Solef P5130, Solvay) with the respective weight ratio of 84:8:8 in an appropriate amount of *N*-methyl-2-pyrrolidone solvent (NMP, anhydrous, Sigma-Aldrich), a homogeneous slurry was obtained. This slurry was cast on an aluminum current collector foil using the doctor blade technique. After the coating was dried, electrodes with 12 mm diameter were punched and dried at 130 °C under dynamic vacuum (2×10^{-2} hPa) in a Büchi glass oven overnight. Alumina-protected CR2032 coin cells (Hohsen) were built using these electrodes as the working electrode, two layers of glass fiber separator (Ø 16 mm, GFA, Whatman), 150 μL of 1 M $NaPF_6$ in a propylene carbonate (PC) electrolyte, and sodium metal foil serving as the counter electrode (Ø 16 mm, Acros Organics). Cycling with various cutoff voltages (1.5−4.3, 2.0−4.3, 1.5−3.8, 2.0−3.8 V) was performed on a multichannel galvanostatic cell test system (CTS, Basytec). In any case, cycling procedures commenced with discharge. GITT measurements were performed on a VMP3 potentiostat (Biologic) within the voltage window of 4.3−1.5 V using specific current pulses of 17.3 mA g^{-1} (C/10) for 10 min. Equilibrium was assumed when the voltage change was <0.0001 V h^{-1}. For impedance study, PAT cells (EL-Cell) are constructed with the same working electrodes,

https://doi.org/10.1021/acs.chemmater.3c01499
Chem. Mater. 2023, 35, 8065−8080

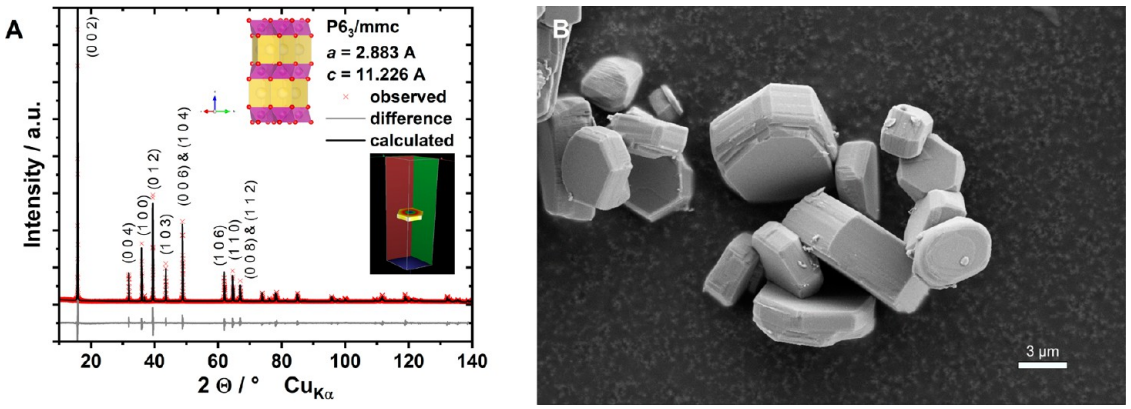

Figure 1. Physical characterization of the P2-$Na_xMn_{3/4}Ni_{1/4}O_2$ cathode active material. (A) Analysis of the XRD pattern using the Rietveld method with depiction of crystal structure and refined anisotropic crystallite size as insets. (B) SEM image.

glass fiber separators with a sodium ring reference electrode (PAT core, EL-Cell), 150 μL of 1 M $NaPF_6$ in PC + 5% FEC electrolyte, and sodium metal foil counter electrodes (Ø 18 mm). A VMP2 potentiostat (Biologic) was used. The temperature was controlled using a climate chamber (CTS GmbH) at 25 °C. Prior to every potentiostatic electrochemical impedance spectroscopy (PEIS) measurement, the cell was allowed to rest for 1 h. PEIS measurements were performed in the frequency range 200 kHz to 5 mHz with 10 mV of amplitude.

Operando Characterization. Operando X-ray synchrotron diffraction measurements were performed at PETRA III, beamline P02.1 (DESY, Hamburg, Germany).[50] An eight-fold coin cell holder, connected to a Biologic Instruments potentiostat, was applied as described elsewhere.[51] A wavelength of 0.20734(1) Å was determined by analysis of positions of reflections of the LaB_6 reference material (NIST 660C). For the characterization of the pristine material, the first diffraction pattern was recorded before starting the electrochemical measurement. Subsequently, the cell was first discharged and then charged at a constant current. All diffraction patterns were analyzed by the Pawley method with TOPAS V6 software. Reflections of the Al current collector served as an internal standard during the measurements, thus providing independent control of the reliability of the obtained model parameters. A differential electrochemical mass spectrometry (DEMS) cell was assembled under an argon atmosphere. Before assembly, all cell parts were dried at 60 °C for at least 12 h. As separators, Whatman GF/A glass microfiber filters were used after drying at 110 °C under vacuum overnight. 1.2 mL of 1 M $NaPF_6$ in PC was used as the electrolyte. The same electrode sheet as described above served as the working electrode. The DEMS cell was constantly flushed with a stream of helium to transfer evolving gases to the mass spectrometer (Pfeiffer Vacuum OMNISTAR GSD320). Before the inlet to the mass spectrometer, the gas stream is passed through a cold trap (−30 °C) to reduce the background from the evaporated electrolyte solvent. A resting time of 24 h was applied before cycling to equilibrate the background signals. The cycling was performed at a constant current of 17.3 mA g^{-1} between 1.5−4.3 V vs a sodium-metal quasi-reference electrode. The full mass spectrum (m/z = 1−100) was measured every 100 s. The gases were quantified from the full spectrum against a calibration matrix, which was measured from calibration gas mixtures of single gases in helium. A detailed description of the setup and the data evaluation will be given in an upcoming publication.

Ex Situ Characterization. For ex situ TEM and XRD investigations, electrodes were cycled in CR2032 coin cells as described above for 3 or 10 cycles, galvanostatically discharged to 2.68 V (equals OCV of pristine cells), followed by a constant voltage step for 5 h and then carefully opened inside an Ar-filled glovebox. The electrode composite was scratched off the aluminum current collector and carefully ground with the mortar and pestle. By discharging to 2.68 V, the sodium stoichiometry of the as-synthesized material was approximately restored, leading to a stable and relatively moisture-insensitive sample. Lamellae for TEM investigations were prepared with a Zeiss NVision 40 Ar (Zeiss Microscope) Ga-ion focused ion beam (FIB) device. The cross-sectional lamellae were prepared along the [11$\bar{2}$0] crystal axis to allow imaging of the crystal stacking in the subsequent TEM investigations. A few micrometer carbon layer was deposited by the gas injection system (GIS) to protect the sample surface. The roughly cut lamella was transferred via a micromanipulator to a standard copper lift-out grid and thinned with decreasing beam currents. End thinning was performed in the low voltage 5 kV mode. Bright-field imaging, selected area electron diffraction (SAED), and aberration-corrected high-resolution transmission electron microscopy (HRTEM) imaging were carried out using an image side C_S-corrected FEI Titan 80−300 operated at 300 kV. High-angle annular dark-field (HAADF) scanning TEM images and drift-corrected energy-dispersive X-ray (EDX) elemental maps were acquired using a Thermo Fisher Talos 200× microscope operated in STEM mode at 200 kV. The intensity of the elemental maps shows the counts according to the background corrected and fitted model. Fast Fourier transformations (FFTs) were performed with Digital Micrograph software (Gatan). The bulk crystal structure after cycling was characterized ex situ using capillary transmission XRD on a D8 Advance (Bruker) diffractometer equipped with a Cu X-ray source and a LynxEyeXE-T detector. For this purpose, the scratched-off electrode composite was filled in 0.3 mm quartz glass capillaries and sealed inside the glovebox. The bulk morphology of the cycled cathode active material was investigated with air-tight cross sections of the cycled electrodes using SEM. Cross sections were polished using Ar-ion beam milling in an IM4000 (Hitachi). SEM investigations were performed on a Leo 1530 VP (Zeiss) with 4 kV acceleration voltage and an Everhart−Thornley SE detector. Any contact with the environment is avoided by the use of air-tight transfer chambers (Kammrath & Weiss). An overview of the electrochemical history of samples for ex situ investigations is presented in Supporting Figure S1.

RESULTS AND DISCUSSION

Elemental analysis of the as-prepared cathode powder was performed by ICP-OES. From the obtained results, the chemical formula $Na_{0.585}Mn_{0.734}Ni_{0.266}O_2$ is calculated, which is in good accordance with our targeted stoichiometry of $Na_{0.58}Mn_{3/4}Ni_{1/4}O_2$. The considerably low sodium content was targeted to minimize surface impurities, such as Na_2CO_3, $NaHCO_3$, or NaOH,[49,52] which will later allow us to correlate transferred charge in electrochemical measurements with the sodium content of the layered oxide. The absence of surface impurities is confirmed by ATR-FTIR measurements as presented in Supporting Figure S2. The bulk crystal structure is analyzed using XRD as presented in Figure 1A and Supporting Figure S3. The diffraction pattern exhibits narrow

https://doi.org/10.1021/acs.chemmater.3c01499
Chem. Mater. 2023, 35, 8065−8080

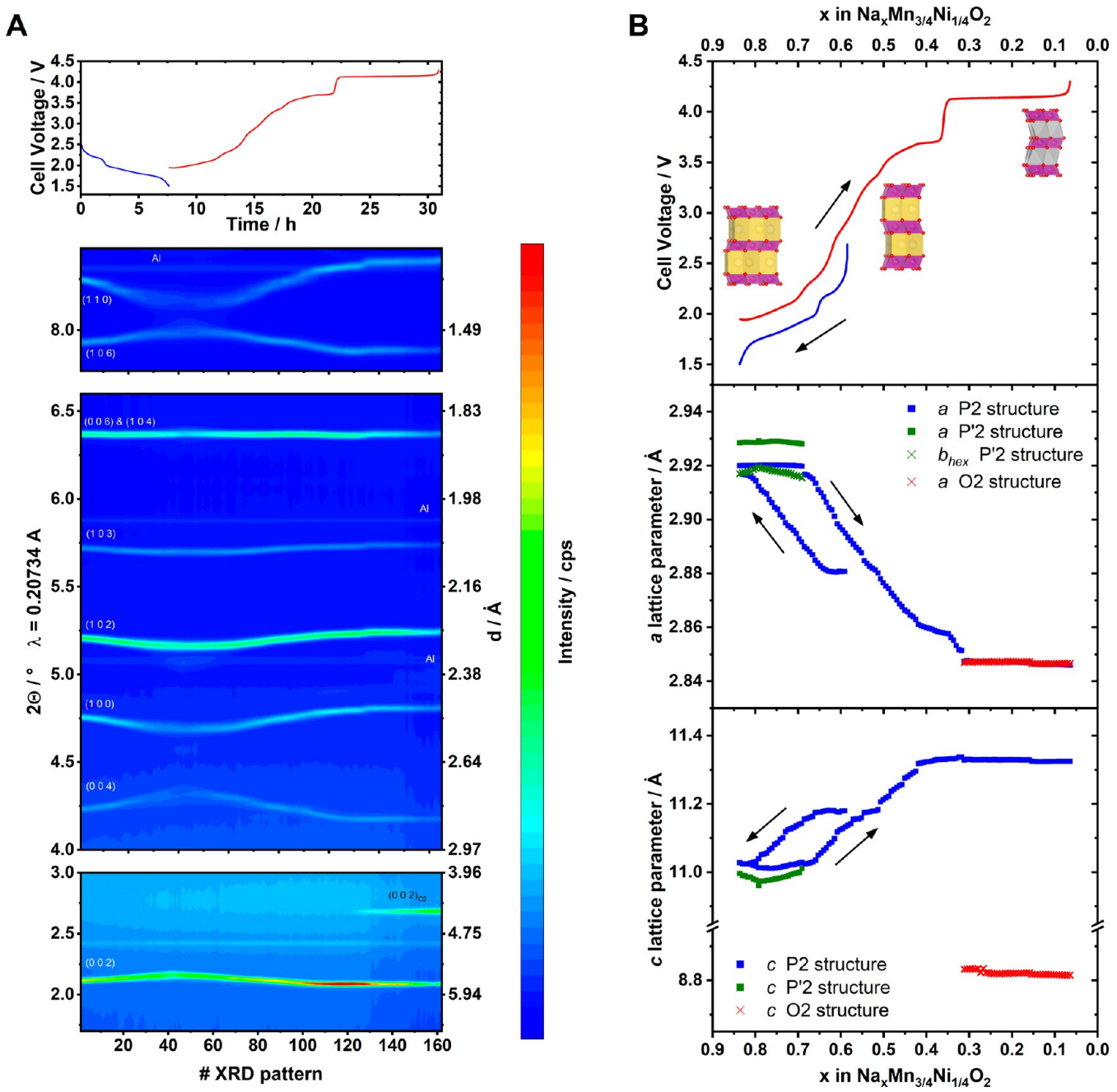

Figure 2. Synchrotron operando XRD of the first cycle. (A) Measured voltage profile and diffraction patterns presented as heat map. (B) Voltage and refined lattice parameters plotted over the calculated sodium stoichiometry. For the P′2 structure, the orthombic *b*-lattice parameter was transformed into the hexagonal system via $b_{hex} = \frac{1}{\sqrt{3}} \cdot b_{orth}$.[56] Depictions of the refined crystal structures are included in the voltage profile.

reflections, indicating high crystallinity, and can be fully indexed with the space group $P6_3/mmc$, indicating the phase-pure nature of P2-type layered sodium transition metal oxides (ICDD01-070-3726). Rietveld refinement resulted in lattice parameters of a = 2.883 Å and c = 11.226 Å. Wyckoff sites and calculated errors of refined parameters are presented in Supporting Table S1. We evaluated the volume-weighted strain and anisotropic crystallite size under the assumption of hexagonal morphology[53−55] by the double Voigt approach. We found a mean anisotropic crystallite size with a diameter of 876 nm in the $a-b$ plane and 170 nm in the c-direction. The strain is as low as e_0 = 0.000261. The powder morphology was investigated with a secondary-electron SEM as presented in Figure 1B. The powder consists of micron-sized particles with a hexagonal platelet-like morphology. The morphology of the particles clearly reflects the hexagonal nature of the layered crystal structure. The crystal size observed in the SEM is in good accordance with the anisotropic crystallite size in the $a-b$ plane as derived from XRD. In the c-direction, on the other hand, crystals appear thicker in SEM images compared to the values obtained from refinement of the XRD pattern, which hints to the fact that a few crystals might be stacked in the c-direction. In fact, we have found grain boundaries within the $a-b$ plane using TEM (compare Supporting Figure S4).

Synchrotron operando XRD was performed to analyze the evolution of the crystal structure of P2-$Na_xMn_{3/4}Ni_{1/4}O_2$

https://doi.org/10.1021/acs.chemmater.3c01499
Chem. Mater. 2023, 35, 8065−8080

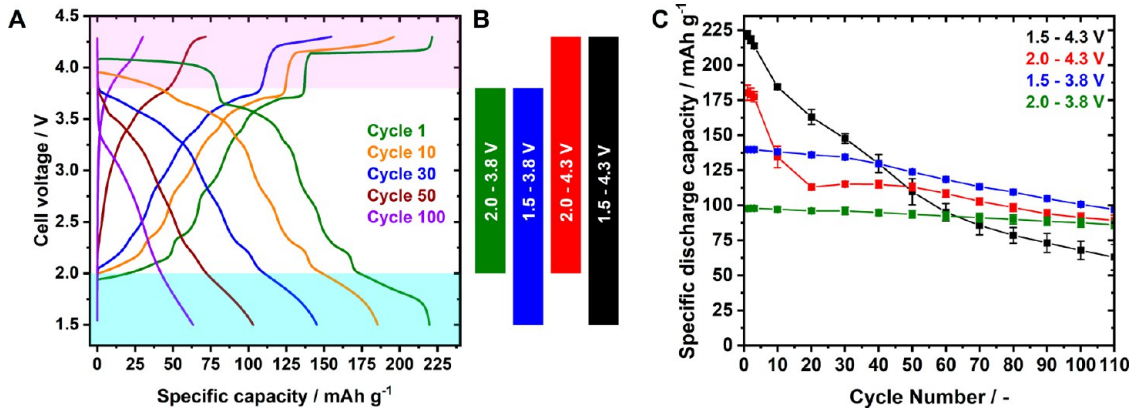

Figure 3. Electrochemical cycling using various voltage cutoffs. Cycles 1, 2, 3, and every tenth cycle are performed at C/10 (17.3 mA g^{-1}) and all other cycles at C/3 (57.7 mA g^{-1}). (A) Voltage profiles for a representative cell cycled within the voltage window of 1.5−4.3 V. (B) Graphic representation of the voltage windows. (C) Specific discharge capacity plotted over the cycle number. Only cycles at C/10 (17.3 mA g^{-1}) are presented. The full cycling data is presented in Supporting Figure S6. Error bars represent the standard deviation of at least two cells.

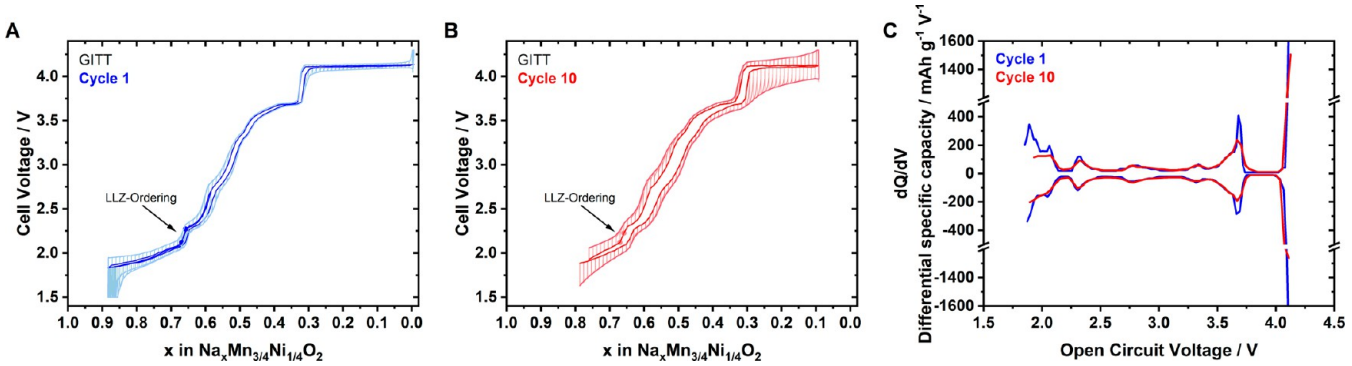

Figure 4. Comparison of GITT measurements in cycle 1 and cycle 10. GITT profile plotted over calculated sodium stoichiometry for (A) cycle 1 and (B) cycle 10. Cycle 10 is aligned using the relaxed voltages based on the voltage shoulder of the "large-zig-zag (LLZ)" ordering at $x = 2/3$. Voltages after relaxation are highlighted in full blue and red colors for cycle 1 and cycle 10, respectively. (C) dQ/dV plot calculated based on the relaxed potentials.

during electrochemical (de)sodiation at room temperature (Figure 2 and Supporting Figure S5). During the initial sodiation (discharge), the *c*-lattice parameter decreases and the *a*-lattice parameter increases. At a high degree of sodiation, a two-phase reaction into an orthorhombic distorted P′2 phase takes place. The distortion most likely results from the presence of Jahn−Teller active Mn^{3+}.[40] In the subsequent desodiation (charge), the system reversibly recedes to the initial P2 structure. The *c*-lattice and *a*-lattice parameters continuously increase and decrease, respectively, indicating a solid solution-like behavior of the P2 structure. At sodium contents $x < 1/3$ ($\gtrsim$4 V), a voltage plateau and the emergence of the second phase (O2) with a decreased *c*-lattice and similar *a*-lattice parameter are detected. Electrochemistry indicates nearly full desodiation of the cathode active material at the end of charge, indicating that the O2 structure most likely is completely desodiated (O2-$Na_0Mn_{3/4}Ni_{1/4}O_2$).[33] During subsequent discharge (sodiation), this P2−O2 two-phase reaction is reversible[42] (not shown here). Please note the P2−O2 phase transition results in an anisotropic reduction of the unit cell volume of approximately 22% from P2-$Na_{1/3}Mn_{3/4}Ni_{1/4}O_2$ to O2-$Na_0Mn_{3/4}Ni_{1/4}O_2$.

Based on this crystallographic evaluation, we can distinguish two different effects, which might contribute to aging of P2-$Na_xMn_{3/4}Ni_{1/4}O_2$, namely, Jahn−Teller distortion due to the presence of Mn^{3+} at low voltage and anisotropic volume change of the P2−O2 two-phase reaction at high voltage. To distinguish these effects, we have cycled cells with various cutoff voltages as presented in Figure 3 and Supporting Figure S6. Independent of the voltage window, cycling procedures commenced with an initial discharge to the respective voltage. For ease of comparison, only cycles at C/10 (17.3 mA g^{-1}) are presented in Figure 3C. The full cycling data is provided in Supporting Figure S6. If the upper cutoff voltage exceeds 3.8 V (utilizing the P2−O2 phase transition), a pronounced capacity fade during the first twenty cycles is observed. If the low cutoff voltage is set below 2.0 V, a gradual capacity decay from cycle 20 onward is detected. If both critical voltage regimes are avoided and the voltage window is limited to 2.0−3.8 V, cycling is relatively stable but with limited specific capacity. Independent of the voltage window, an increasing difference between the specific capacity at slow (C/10 = 17.3 mA g^{-1}) and faster (C/3 = 57.7 mA g^{-1}) cycles is apparent, hinting toward decreasing cell kinetics upon cycling (Supporting Figure S6). At high specific currents, the sodium metal counter electrode can be significantly polarized.[57] To avoid any misinterpretations due to any potential influence of the sodium metal counter electrode, only cycles at C/10 are discussed throughout the manuscript. Additionally, the improved resolution of the voltage steps at low specific currents (C/10) allows differential capacity analysis. dQ/dV analysis for cycle 1, cycle 10, and cycle 100 is presented in Supporting

https://doi.org/10.1021/acs.chemmater.3c01499
Chem. Mater. 2023, 35, 8065−8080

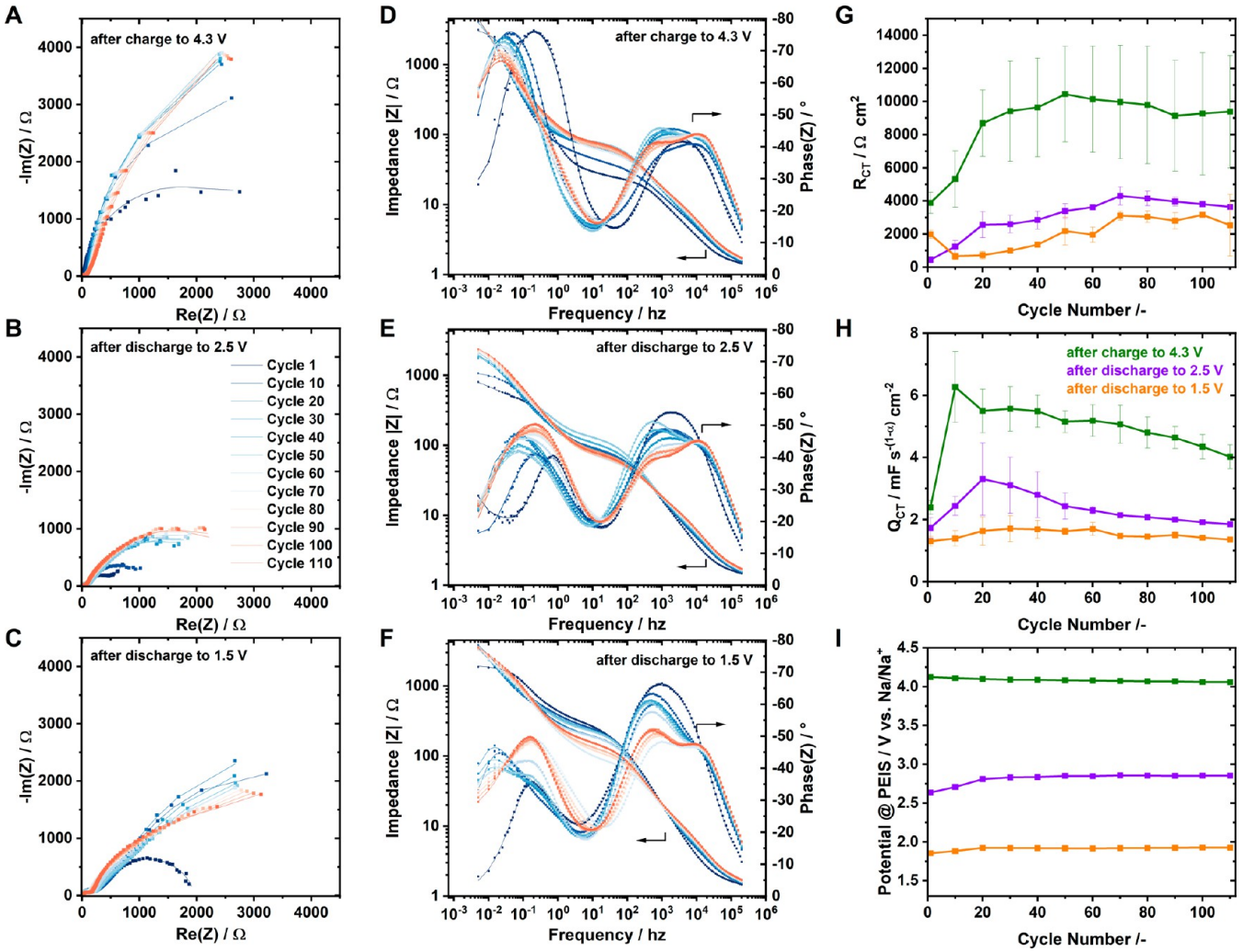

Figure 5. Impedance study. (A–C) Nyquist plots after charge to 4.3 V, discharge to 2.5 V, and discharge to 1.5 V, respectively. (D–F) Bode plots after charge to 4.3 V, discharge to 2.5 V, and discharge to 1.5 V, respectively. (G) Course of charge transfer resistance (R_{CT}) and (H) Q_{CT} over cycling as derived from the fitting of impedance spectra. (I) Potentials at which PEIS measurements are performed after charge to 4.3 V, discharge to 2.5 V, and discharge to 1.5 V (all followed by 1 h of relaxation before PEIS measurements). In Nyquist and Bode plots, the obtained measurement data is presented as dots, and corresponding fittings are presented as lines. In panels (G)–(I), error bars represent the standard deviation of the respective values for three independent cells.

Figure S7. When the charging voltage exceeds 3.8 V, the capacity fade during the first ten cycles is mainly associated with a loss of capacity at high voltage (P2–O2 phase transition). For cycle 100, the high voltage plateau completely vanishes and all signals in the dQ/dV plot are diminished and slightly shifted in voltage, indicating an increase of polarization and a loss of utilizable active material due to complete electronic disconnection of corresponding parts of the active material (in the following referred to as the "loss of active material"). For the 1.5–3.8 V voltage window, no significant change in the dQ/dV plot is observed for cycle 1 and cycle 10. For cycle 100, all signals are decreased in intensity and shifted in voltage, again hinting at a loss of active material and an increase in cell polarization. For the narrow voltage window of 2.0–3.8 V, only a slight shift in voltage is observed in the dQ/dV plot during 100 cycles, indicating a minor increase in cell polarization but no loss of active material. Overall, the pronounced capacity fade over the first 20 cycles is dominated by a decreasing utilization of the high voltage plateau (P2–O2 phase transition), whereas the subsequent cycles show a slower capacity fading associated with the utilization of the low voltage region (Jahn–Teller effect).

To distinguish between nonkinetic aging effects (e.g., loss of capacity, which remains inaccessible even under infinitely low current, such as mechanical/electrical isolation of active material or transformation toward electrochemically inactive phases) and kinetic aging effects (e.g., cell polarization caused by CEI growth and/or surface densification), we have performed GITT measurements in cycle 1 and cycle 10 (Figure 4A,B). Between these cycles, the cells followed the same cycling procedure as described above. The voltages after relaxation (OCV) are highlighted with a blue and red hull curve for cycle 1 and cycle 10, respectively. For the GITT measurement in cycle 10, we used the voltage shoulder of the large-zig-zag Na^+/vacancy ordering (LLZ) at $x = 2/3$ to align the OCV hull curves of both GITT measurements at this point (x-offset). Both OCV hull curves are in good agreement, indicating that the structure of the pristine material is preserved, and no additional electrochemically active phases arise over the first ten cycles. However, utilization of the

https://doi.org/10.1021/acs.chemmater.3c01499
Chem. Mater. 2023, 35, 8065–8080

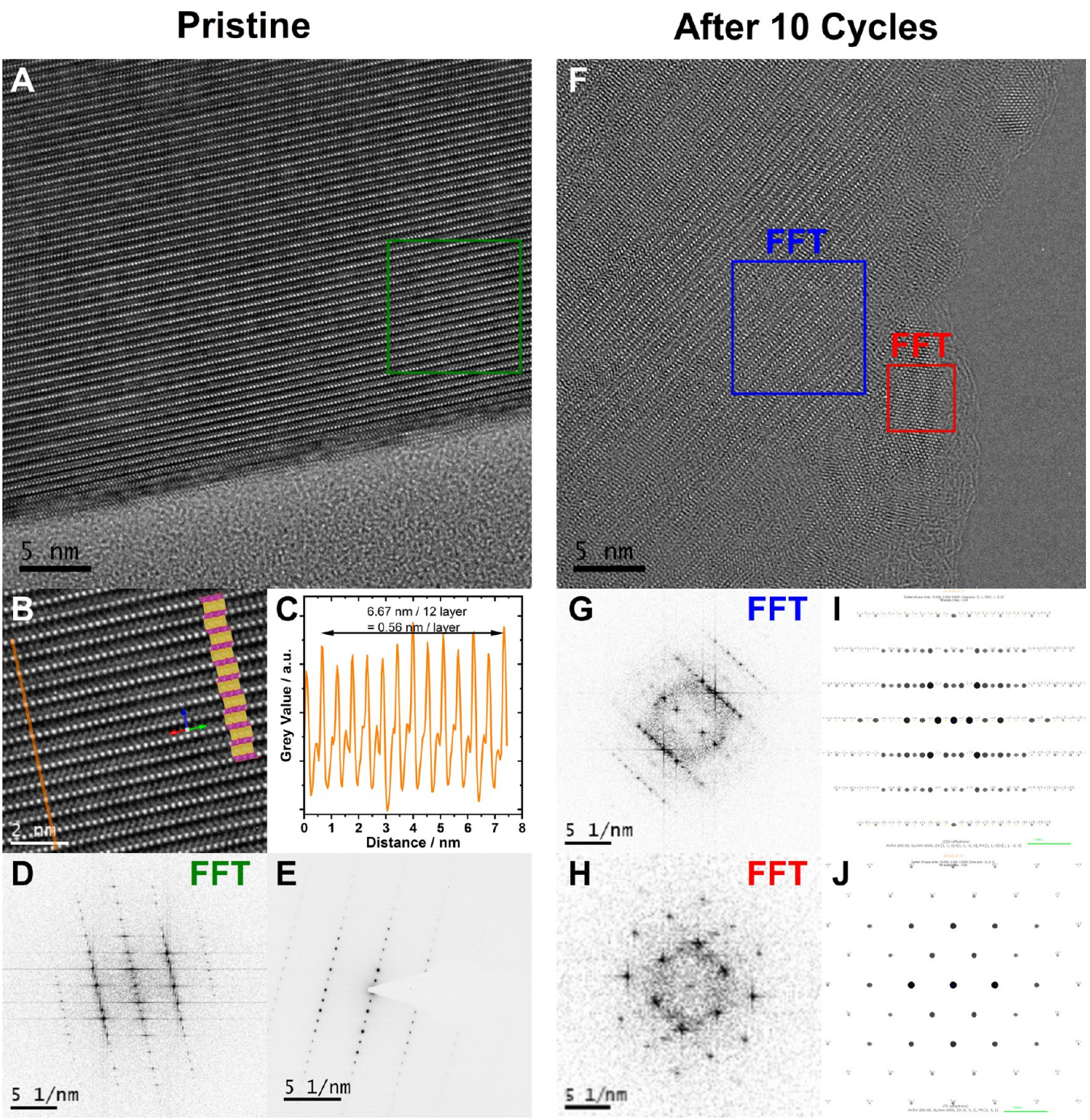

Figure 6. TEM images of pristine P2-$Na_{0.58}Mn_{3/4}Ni_{1/4}O_2$ material (A–E) and material after 10 cycles with similar sodium content (F–H): (A) Aberration-corrected HRTEM image of the pristine material along the [11$\bar{2}$0] zone axis, (B) Magnification of image A (green box), crystal structure as derived from XRD is included as overlay in panel (B), (C) line profile derived along the orange line in image B, (D) FFT of the area marked with a green box in panel (A), (E) selected area electron diffraction derived from a different lamella of the pristine material, (F) aberration-corrected HRTEM image of the material after 10 cycles, (G) FFT of the area marked with a blue box in panel (F), (H) FFT of the area marked with a red box in panel (F), (I) calculated kinematic diffraction pattern of P2-$Na_{0.58}Mn_{3/4}Ni_{1/4}O_2$ along [11$\bar{2}$0], and (J) calculated kinematic diffraction pattern of NiO along [110].

(de)intercalation capability is limited in cycle 10, which is supported by the differential specific capacity plot derived from the relaxed voltages (dQ/dV_{OCV}), as presented in Figure 4C. Comparing the on-load voltage profile of the GITT measurements (C/10 = 17.3 mA g^{-1}), we find significant state of charge (SOC)-dependent differences between cycle 1 and cycle 10. At a high SOC (≥ 3.8 V), the initially small polarization within the P2–O2 two-phase region is significantly increased in cycle 10. During charge of cycle 10, polarization is continuously increasing with advancing transformation from P2 to O2, leading to a sloping voltage profile and limited desodiation of the electrode. During the subsequent discharge of cycle 10, polarization is significantly higher during discharge than in the previous charge, leading to a sloping voltage profile under the current load. A hysteresis in the *x*-direction between charge and subsequent discharge is

https://doi.org/10.1021/acs.chemmater.3c01499
Chem. Mater. 2023, 35, 8065–8080

apparent, which is more pronounced in cycle 10 than in cycle 1, hinting toward more pronounced side reactions, such as electrolyte oxidation in cycle 10. At an intermediate SOC (2.0−3.8 V), only a slight increase in polarization from cycle 1 to cycle 10 is apparent. At a low SOC (<2.0 V), polarization in cycle 10 is significantly higher than polarization in cycle 1, limiting sodiation of the electrode during discharge. Overall, the comparison of GITT in cycle 1 and cycle 10 provides strong evidence for a SOC-dependent increase of polarization, which contributes to the pronounced capacity fade during the first 10 cycles of P2-$Na_xMn_{3/4}Ni_{1/4}O_2$. No indication of irreversible loss of active material within the first 10 cycles is observed.

To further investigate the kinetic effects, impedance measurements (PEIS) in a three-electrode setup were applied. PEIS measurements at various SOC during the first charge half-cycle are presented in Supporting Figure S9. During cycling, the impedance of the P2-$Na_xMn_{3/4}Ni_{1/4}O_2$ working electrode was measured every tenth cycle after charge to 4.3 V, after discharge to 2.5 V, and after discharge to 1.5 V, all at C/10 (17.3 mA g^{-1}), as presented in Supporting Figure S8. The obtained Nyquist and Bode plots of a representative cell are presented in Figure 5A−F. Nyquist plots consist of a small arc at a high frequency and a larger one at a low frequency. The respective Bode plots show a bimodal peak of the phase shift with a simultaneous increase of the absolute impedance in the high-frequency regime (200 kHz to 10 Hz) as well as a peak of the phase shift with a simultaneous increase of absolute impedance at low frequencies (1 Hz to 5 mHz). In battery research, arcs in the Nyquist plot in combination with a simultaneous increase of absolute impedance and a peak of the phase shift in the Bode plot are typically associated with electrodes in contact with the electrolyte.[58−60] The submerged electrode exhibits a capacitive behavior in parallel with a charge transfer resistance, which can be modeled using a simplified Randles circuit consisting of a capacitor (C) in parallel with a resistor (R).[58,60,61] To account for nonideal capacitive behavior (e.g., due to electrode roughness), the capacitor can be substituted by a constant phase element (CPE).[62−66] Based on our findings, we apply an equivalent circuit, as presented in Supporting Figure S10, to fit the obtained impedance spectra. The equivalent circuit consists of a high-frequency resistance (R_{HF}) to account for electronic contacts and ionic transport resistance in series with three modified Randles circuits (R_i||CPE$_i$). Additionally, in the first cycles after discharge to 2.5 V, measurements show an approximately 45° slope in the Nyquist plot as well as increasing absolute impedance and a constant phase shift at very low frequencies, which is typically fitted using a Warburg element (W_{diff}) to account for diffusion processes.[58,60,67] This Warburg element is only applied to the fitting, where clear signs of Warburg diffusion are found in impedance spectra. Based on the characteristic time constants, the three Randles circuits are assigned to (i) contact impedance ($\tau \approx 10^{-5}$ s),[68−71] (ii) transport through CEI ($\tau \approx 10^{-3}$ s),[70,71] and (iii) charge transfer ($\tau \approx 0.1-10$ s).[70,72,73] Upon cycling, impedance measurements after discharge to 1.5 V indicate an additional process at low frequency (R_{CT2}||CPE$_{CT2}$). So far, the physical interpretation of this process remains elusive and the corresponding discussion is provided in the Supporting Information. Fitting results are presented in Figure 5G,H and Supporting Figure S11. The actual potentials after relaxation, at which PEIS measurements are performed, are plotted in Figure 5I. After charge to 4.3 V, the potentials at which PEIS is measured remain almost constant throughout cycling, in accordance with the two-phase P2−O2 voltage plateau (compare Figure 4). After discharge to 2.5 V and 1.5 V, the rest potentials at which PEIS is measured increase within the first 20 cycles in accordance with increasing polarization and remain almost constant for the following cycles. Charge transfer resistance (R_{CT}) derived from the fitting of impedance spectra is presented in Figure 5G. R_{CT} is the highest at a high SOC, which is in accordance with polarization at high voltage in GITT measurements and reports in the literature.[57] For high and intermediate SOCs, R_{CT} increases rapidly (approximately triples) during the first 20 cycles and then remains approximately constant at a high level. The increase in charge transfer resistance is in accordance with increasing polarization upon cycling as observed in GITT measurements (Figure 4) and dQ/dV analysis (Supporting Figure S7). The parameter Q of a constant phase element (CPE) can serve as an indicator for the double-layer capacitance[57,74] and is plotted in Figure 5H. After charge to 4.3 V, Q_{CT} approximately triples within the first 10 cycles, followed by a slight decrease in the subsequent cycles, indicating a significant increase of double-layer capacitance after charge to 4.3 V. A similar trend is observed after discharge to 2.5 V, but to a much lesser extent. After discharge to 1.5 V, Q_{CT} remains almost constant during cycling, indicating little to no change of the double-layer capacitance. Additional information regarding PEIS evaluation is provided in the Supporting Information and in Supporting Figure S11.

Overall, our impedance study provides further evidence for (i) a continuous SOC-independent increase of polarization, (ii) a SOC-dependent drastic increase of charge transfer resistance at high SOC during the first 20 cycles, and (iii) an SOC-dependent change of double-layer capacitance at high voltage (high SOC).

Ex situ aberration-corrected (AC) HRTEM was performed to investigate local changes on the pristine and cycled material (after 10 cycles), respectively. The hexagonal morphology of the single-crystal particles (see Figure 1B), which reflects the hexagonal crystal structure of the P2-$Na_xMn_{3/4}Ni_{1/4}O_2$ material, allowed us to prepare TEM lamellae with an orientation along the $[11\bar{2}0]$ zone axis. Representative AC-HRTEM images of the pristine material and the material after 10 cycles are presented in Figure 6A,B,F, respectively. For the pristine material, lattice fringes of the layered structure are clearly visible in the AC-HRTEM images. In Figure 6B, a depiction of the crystal structure as derived from XRD is included to illustrate the orientation of the $[11\bar{2}0]$ zone axis. Analysis of the line intensity profile in the c-direction is in good accordance with the interlayer distance as derived from XRD (Figure 6C). Fast Fourier transformation (FFT) within the area marked by the green box is presented in Figure 6D, showing the crystal structure. Selected area electron diffraction (SAED) of a different TEM lamella is presented in Figure 6E, where the spatial frequencies of the reflections are in good agreement with the lattice fringes derived from the FFT shown in Figure 6D. The intensity of the SAED pattern is in good accordance with the calculated kinematic diffraction pattern for the hexagonal structure (Figure 6I), confirming the bulk structure on a local level. The layered structure is maintained from bulk close to the surface of the particle (Figure 6B). After 10 cycles, HRTEM images show lattice fringes of the layered structure in the bulk and an approximately 5−10 nm thick surface film consisting of nanometer-sized, crystalline areas

https://doi.org/10.1021/acs.chemmater.3c01499
Chem. Mater. 2023, 35, 8065−8080

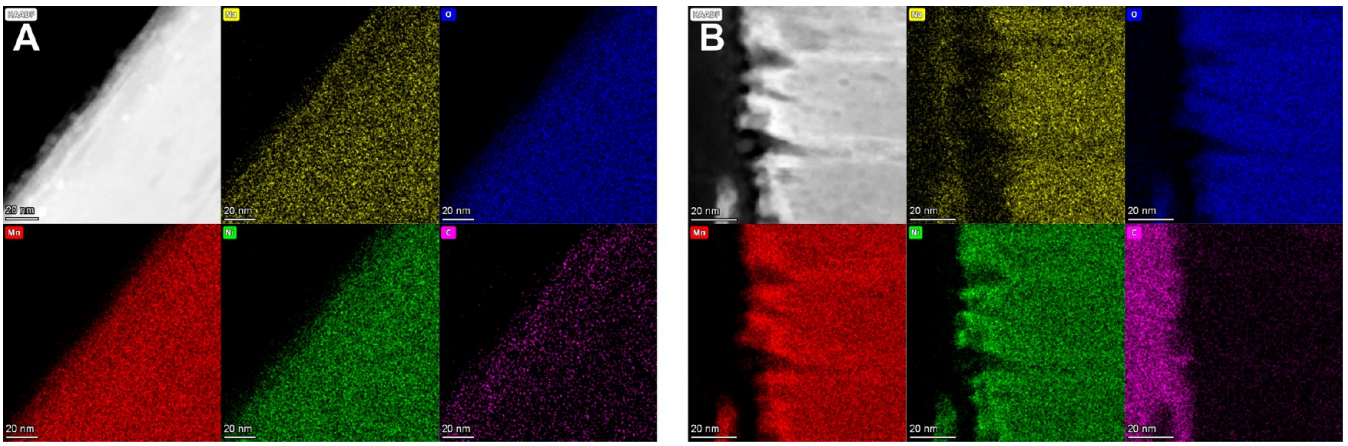

Figure 7. HAADF image and EDX mapping of the surface near regions in TEM lamellae of (A) pristine material and (B) material after 10 cycles. Sodium is depicted in yellow, oxygen in blue, manganese in red, nickel in green, and carbon in magenta color.

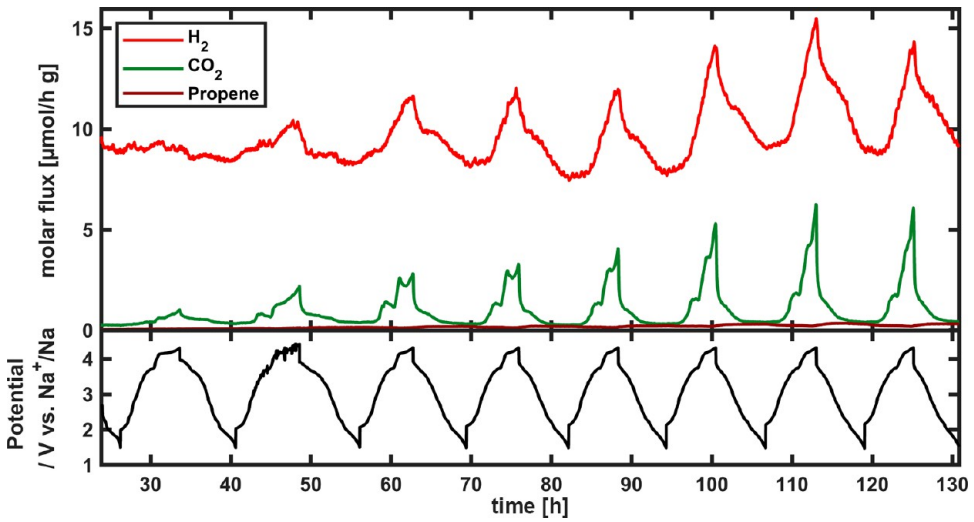

Figure 8. DEMS measurement over the first eight cycles in a voltage window of 1.5−4.3 V.

with different lattice fringes (Figure 6F). The FFT in the bulk area (blue box) shows the same lattice fringe pattern as in Figure 6D, confirming the layered structure in the bulk of the cycled material (Figure 6G,I), in accordance with ex situ capillary XRD patterns as presented in Supporting Figure S13. The FFT in the surface near region (red box) results in a pattern, which matches very well with the calculated diffraction pattern of cubic NiO along the [110] zone axis (Figure 6H,J). After 10 cycles, we have found this surface film on all surfaces exposed to the electrolyte on several TEM lamellae. The cubic nature of nanometer-sized particles similar to NiO or MnO is confirmed by FFTs for several areas and on various TEM lamellae. Additionally, we observed severe cracking in the $a-b$ plane of the active material (Supporting Figure S14). The surfaces of these cracks exhibit similar surface films.

Energy-dispersive X-ray (EDX) mappings, using scanning (S)TEM imaging of the pristine and cycled material (after 10 cycles), are presented in Figure 7A,B, respectively. As described in the Experimental Section and illustrated in Supporting Figure S1, the cycled material was harvested from electrodes after discharge to 2.68 V, resulting in similar sodium content in the layered oxide compared to the pristine material. For the pristine material, a homogeneous distribution of the elements Na, Mn, Ni, and O is observed. After 10 cycles, an increased contrast in the surface near region is observed in the high-angle annular dark-field (HAADF) STEM image, which indicates either heavier elements or a denser structure in the surface near region.[75] This surface near region is enriched in Mn and Ni and poor in Na. In the bulk of the cycled material, Na, Mn, Ni, and O are distributed evenly. A Na- and C-containing film sits on top of this transition metal-enriched dense surface film, which might be related to the carbon binder domain of the electrode composite or originate from oxidative electrolyte decomposition (CEI products). A second set of EDX mappings for the pristine material after 3 cycles and after 10 cycles is provided in Supporting Figure S12.

Overall, HRTEM images and STEM-EDX mappings suggest the formation of a dense, 5−10 nm thick film on the surfaces exposed to the electrolyte during cycling. EDX mappings show that this surface film is rich in transition metals and contains no (or very little) Na. FFTs indicate that the surface film exhibits nanoparticles with a cubic structure similar to NiO or MnO. Additionally, EDX mappings provide evidence for the formation of a CEI. Please note that the density of NiO (ρ = 6.807 g cm^{-3} ICDD00-047-1049) and MnO (ρ = 5.361 g cm^{-3} ICDD01-075-6876) is considerably higher compared to P2-$Na_{0.58}Mn_{3/4}Ni_{1/4}O_2$ (ρ = 4.141 g cm^{-3}). All of these findings are consistent with surface densification on layered

https://doi.org/10.1021/acs.chemmater.3c01499
Chem. Mater. 2023, 35, 8065−8080

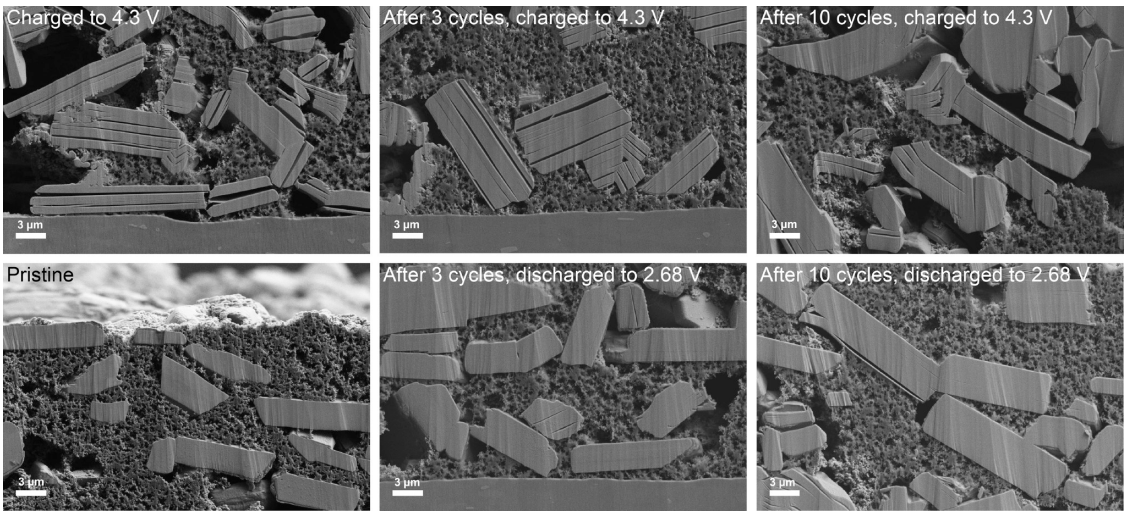

Figure 9. Air-tight SEM cross-sectional images illustrating the particle cracking phenomena.

oxide cathodes for LIBs (e.g., NCM, NCA), indicating that a high degree of sodium de-intercalation results in oxygen release, reduction of transition metals, and formation of dense surface films with a cubic rock salt structure (e.g., NiO). In LiBs, signs for surface densification are typically reported for Ni-rich NCMs, when more than 80% of Li is removed from the alkali metal layer.[1,76−80] For $LiNiO_2$, the overall reaction for surface densification can be written as[81]

$$Li_xNiO_2 \rightarrow xLi^+ + xe^- + NiO + \frac{1}{2}O_2$$

Based on our findings, we propose a similar reaction to happen during cycling (repeated full desodiation) on the surface of the P2-$Na_xMn_{3/4}Ni_{1/4}O_2$ cathode active material

$$Na_xMO_2 \rightarrow xNa^+ + xe^- + MO + \frac{1}{2}O_2$$

To check for further signs of oxygen release during cycling, we have performed DEMS measurements (Figure 8). Released lattice oxygen is directly detected in some DEMS studies.[44,82,83] In other reports, oxygen release from active materials is also detected as CO_2 or CO due to the direct chemical reaction of released oxygen species with electrolyte or conductive carbon.[76−78,82,84] In the measurements presented in this work, no direct oxygen release was observed. During the first cycle of our DEMS experiment, no significant gas evolution is detected until the cathode potential exceeds 3.8 V. The small amounts of H_2 and CO_2 evolution detected before the cell reaches 3.8 V can be attributed to the reaction of the electrolyte with the sodium metal counter electrode. With the onset of the P2−O2 phase transition (≥3.8 V), CO_2 evolution is detected, which is continuously increasing until the end of charge. During the subsequent discharge, the CO_2 evolution decreases. In the following, no gas evolution is detected until the cathode potential reaches approximately 3.3 V in the subsequent charge of cycle 2. At this point, small amounts of H_2 and CO_2 are detected, which are most likely related to the decomposition of an acidic product originating from oxidative electrolyte decomposition.[85−87] When the cathode potential exceeds 3.8 V in the second cycle, CO_2 and H_2 evolution are detected once more. The following cycles undergo a similar course of gas evolution with increasing amounts of gases. The CO_2 peak during charging at potentials ≥3.8 V is clearly bimodal in cycles three to five, with the first maximum located at the onset of the phase transition from P2 to O2 and the second maximum at the end of charge. Under the assumption that oxygen release from $Na_xMn_{3/4}Ni_{1/4}O_2$ most likely occurs at a high degree of desodiation, similar to layered lithium transition metal oxides (e.g., NCM, NCA),[77,78] the oxygen release must be related to the O2 phase ($Na_0Mn_{3/4}Ni_{1/4}O_2$). Under constant current charging, it is reasonable for the P2−O2 phase transition to start on the surface of the cathode active material, potentially leading to the release of CO_2 arising from the reaction of released lattice oxygen species with the electrolyte and resulting densification of the cathode active material subsurface. At the end of charge, most of the cathode active material has undergone the P2−O2 phase transition, which results in a substantial anisotropic volume reduction of 22%. This volume change potentially causes cracking of the cathode active material, exposure of new surfaces to the electrolyte, and subsequently, new surfaces, which might be subject to the release of oxygen species and surface densification. Therefore, continuous increase of surface area due to cracking can rationalize the increasing gas evolution during cycling. The detection of released lattice oxygen in the form of CO_2 due to the chemical reaction of the reactive oxygen species with the electrolyte is supported by an increasing R_{CEI} in impedance measurements (Supporting Figure S11) and would be in accordance with potential CEI products in EDX measurements (Figure 7B).

To further investigate cracking of our $Na_xMn_{3/4}Ni_{1/4}O_2$ cathode active material, we have performed air-tight SEM cross sections of electrodes in the pristine state, cycle 1, cycle 3, and cycle 10 after charging to 4.3 V and discharging to 2.68 V, respectively (Figure 9). The pristine electrode shows dense particles. A direct discharge of the pristine electrode to 1.5 V has no influence on the particle morphology (Supporting Figure S15). After direct charge to 4.3 V, clear cracks in the *a*−*b* plane of the active material are apparent. After three and ten cycles, cracking can be observed after charging to 4.3 V. After subsequent discharge to 2.68 V, particles appear dense, indicating reversibility of crack formation with respect to the resolution of SEM. However, TEM lamellae prepared from the same cycled samples exhibit distinct cracks in the *a*−*b* plane when investigated with the higher resolution of TEM (Supporting Figure S14). We therefore suggest that hundreds

https://doi.org/10.1021/acs.chemmater.3c01499
Chem. Mater. 2023, 35, 8065−8080

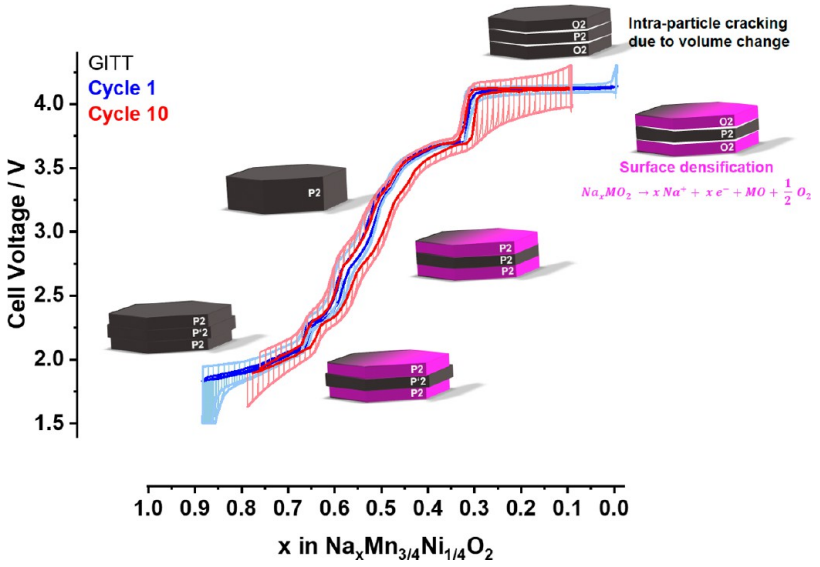

Figure 10. Graphic summary of aging phenomena detected in this work.

of nanometer-wide cracks formed in charged samples narrow during subsequent sodiation, resulting in a few nanometer-wide cracks after discharge to 2.68 V. With decreasing width of the cracks, the contact area between particle fragments potentially increases, eventually resulting in electronic re-contacting during discharge. Due to the observed reversibility of cracking, we assume that cracks do not fully penetrate the single-crystalline particles but instead remain partially connected allowing heal up of the cracks. The observation of SOC-dependent cracking is in accordance with SOC-dependent increase of double-layer capacitance as indicated by PEIS. In the charged state (4.3 V), the degree of cracking observed in SEM electrode cross sections seems to decrease from cycle 1 to cycle 10, which is in accordance with the decreasing utilization of the P2−O2 phase transition during cycling (compare Figure 4). To quantify the extent of cracking, further experiments such as impedance measurements in blocking conditions or ex situ physisorption would be necessary.[74,88,89]

Overall, P2-$Na_xMn_{3/4}Ni_{1/4}O_2$ cathode materials for sodium-ion batteries suffer from capacity fading upon cycling in half-cells with the voltage range of 1.5−4.3 V. The significant capacity fading in the first twenty cycles is mainly associated with decreasing utilization of the high voltage P2−O2 phase transition. From GITT and impedance measurements, we find evidence for a SOC-independent general increase of polarization and a SOC-dependent increase of polarization at a high SOC, both contributing to capacity fading. Upon prolonged cycling, some capacity is lost due to the loss of active material caused by mechanical stress arising from an orthorhombic distortion due to Jahn−Teller active Mn^{3+} at low voltage.

After repeated charging to high voltage, HRTEM and EDX provide clear evidence of surface densification on cycled P2-$Na_xMn_{3/4}Ni_{1/4}O_2$. The resulting rock salt structures (e.g., NiO, MnO) are poor electronic conductors[90] and lack the necessary diffusion paths for ionic transport of alkali metals,[91] resulting in an SOC-independent increase of polarization. Furthermore, the release of oxygen species during surface densification leads to electrolyte oxidation and gas formation in accordance with DEMS measurement. In O3-type layered LIB cathode active materials, such as Ni-rich NCMs, surface densification is reported to proceed via a spinel-type intermediate structure due to the migration of Ni ions from the transition metal layer to the lithium layer.[1,81] For SIBs, similar surface densification resulting in NiO-like surface layers was reported for O3-type $NaNi_{1/2}Mn_{1/2}O_2$ cathode materials.[92] For P2-type cathode active materials, the transformation to a spinel-type intermediate structure is unlikely from a structural point of view due to the particular oxygen stacking sequence of P2-type materials.[93] Additionally, sodium-containing spinel-type structures are reported to be thermodynamically unstable.[94−96] Therefore, we suggest that surface densification in P2-type sodium layered oxides might follow a different mechanism. Instead of the above-described structural pathway to surface densification, an electronic pathway via the oxidation of oxygen,[43,44,97] release thereof from the near-surface structure, and subsequent surface densification might be possible. Further investigations to clarify the reaction mechanism toward surface densification will be necessary in the future.

At a high SOC and for cycled cathode active material, cracks in the $a-b$ plane are observed using TEM lamellae and SEM electrode cross sections. Such cracking upon charge of the cathode active material can cause partial electronic disconnection for active material particle fragments, resulting in poor electronic connection for these fragments. Under the power load, the resistance of the electronic pathway toward these particle fragments results in increased overpotentials. Macroscopically, the difference in electronic connection for a large number of particle fragments potentially causes the observed sloped galvanostatic potential profile for the P2−O2 phase transition as observed in cycle 10. The increasing resistance is in accordance with the SOC-dependent increase of polarization at high voltage as observed in GITT and impedance measurements. Upon repeated cracking, some parts of the cathode active material might be completely electronically disconnected, leading to a loss of active material. These findings are summarized in Figure 10.

Therefore, our findings can explain the SOC-independent increase of polarization due to surface densification and the SOC-dependent increase of polarization at high voltage due to cracking of the active material as well as the observed capacity loss after prolonged cycling due to the loss of active material.

https://doi.org/10.1021/acs.chemmater.3c01499
Chem. Mater. 2023, 35, 8065−8080

Further investigations to elucidate the SOC-dependent increase of polarization at low voltage are currently ongoing.

CONCLUSIONS

In this work, we have investigated the origin of capacity fading of micron-sized single-crystalline P2-$Na_xMn_{3/4}Ni_{1/4}O_2$ model material as the cathode for sodium-ion batteries. Using HRTEM and EDX, we identified surface densification as the possible cause for increasing polarization (SOC-independent). The occurrence of surface densification is supported by DEMS. Furthermore, we identified partly reversible cracking due to the significant volume change of the P2−O2 phase transition as a cause for SOC-dependent increase of polarization at high voltage. The aging behavior observed in this study is in good accordance with many reported P2-type sodium layered oxides, in particular P2-$Na_xMn_{1-y}Ni_yO_2$ materials,[38,39,41,42,44] which suggests that our findings are not limited to the particular stoichiometry, but are rather a common phenomenon in this material class. Even though a couple of publications have provided indirect evidence for surface densification upon prolonged cycling of P2-type sodium layered oxides,[38,82,97−99] direct proof of surface densification in the literature is scarce. Zhang et al.[44] provide an indication for oxygen redox in P2-$Na_xNi_{1/3}Mn_{2/3}O_2$, observe small amounts of oxygen release in DEMS, and demonstrate a three-layer thick (<1 nm) homogeneous densified surface layer via TEM. Using computational methods, a structure for the densified surface is proposed ($Ni_2Mn_2O_7$). In this work, we provide direct proof of surface densification in P2-type $Na_xNi_yMn_{1-y}O_2$ cathodes for SIBs using HRTEM and EDX and demonstrate the cubic rock salt structure of the nanoparticles within this surface film. The 5−10 nm thick, dense surface film consists of NiO and MnO nanoparticles. To the best of our knowledge, this is the first report providing clear evidence for composition and structure of surface densification on P2-type sodium layered oxide cathode materials for SIBs. For polycrystalline O3-type $NaNi_{1/2}Mn_{1/2}O_2$ cathode materials for SIBs, similar cracking behavior and comparable surface densification resulting in NiO-like surface films are reported.[92] In terms of thickness and NiO-like cubic structure of surface densification, our findings for P2-type $Na_xMn_{3/4}Ni_{1/4}O_2$ and the report on O3-type $NaNi_{1/2}Mn_{1/2}O_2$[92] agree well with reports on Ni-rich NCMs in LIBs.[1,76−81] However, in contrast to Ni-rich NCMs, we do not find any spinel-type intermediate phase. This finding is discussed with respect to the oxygen stacking in P2-type layered oxides and the thermodynamic stability of spinel-type alkali metal oxides. We hope our findings will spark further mechanistic investigations into the formation of surface densification in P2-type alkali metal layered oxides.

ASSOCIATED CONTENT

Supporting Information

The Supporting Information is available free of charge at https://pubs.acs.org/doi/10.1021/acs.chemmater.3c01499.

Additional information for impedance measurements (PEIS) Supporting Figure S1. Illustration of electrochemical history of samples for ex situ characterization. SEM denotes samples for air-tight SEM electrode cross sections, TEM denotes samples for (AC)HRTEM investigations, EDX denotes samples for EDX mappings of TEM lamellae, XRD denotes ex situ capillary XRD measurements. A detailed description of the electrochemical procedure is entailed in the experimental section of the manuscript. Supporting Figure S2. ATR-FTIR spectra of cathode active material powder and NaOH, $NaHCO_3$ and Na_2CO_3 reference materials. (A) 400−4000 cm^{-1} and (B) zoom-in at 400−2000 cm^{-1}. Supporting Figure S3. Zoom into Rietveld Refinement as presented in Figure 1A. Supporting Table S1. Rietveld refinement results and Wyckhoff sites. B_{iso} values are are based on ref 100. Supporting Figure S4. TEM image of lamella prepared from pristine material. A grain boundary in $a-b$ plane between two single crystals is visible. The crystalline nature of both crystallites was confirmed with SAED (not shown here). Supporting Figure S5. Waterfall diagram of obtained diffraction patterns from synchrotron operando XRD with corresponding galvanostatic voltage profile. Diffraction patterns and voltage curve of initial discharge is presented in blue color, subsequent charge is presented in red color. Supporting Figure S6. Specific discharge capacity over course of cycling for various voltage regimes. Cycles 1, 2, 3 and every tenth cycle are performed at C/10 (17.3 mA g^{-1}), all other cycles at C/3 (57.7 mA g^{-1}). (A) 1.5−4.3 V, (B) 2.0−4.3 V, (C) 1.5−3.8V and (D) 2.0−3.8 V. The standard deviation of at least two cells is presented as error bars. Supporting Figure S7. dQ/dV plots for cells cycled at various cutoff voltages for cycle 1, cycle 10 and cycle 100 with voltages windows of (A) 1.5−4.3 V, (B) 2.0−4.3 V, (C) 1.5−3.8 V and (D) 2.0−3.8 V. Supporting Figure S8. Cycling procedure for potentiostatic electrochemical impedance spectroscopy (PEIS) study. Every tenth cycle is performed at 17.3 mA g^{-1} (C/10, blue line), all other cycles are performed at 57.6 mA g^{-1} (C/3, red line). After galvanostatic charging/discharging to the respective potential, the cells were kept allowed to relax for 1 h to guarantee equilibrium before PEIS measurements. Supporting Figure S9. Impedance measurements (PEIS) at various state of charge for a representative cell. (A) Nyquist plot and (B) Bode plot. Supporting Figure S10. Equivalent circuits as applied to fit the obtained impedance data. Supporting Figure S11. Additional information for fitting of impedance data (PEIS). The applied equivalent circuits are presented on the top. (A) Potential at which PEIS measurements were performed, (B) high-frequency resistance, (C) contact resistance, (D) CEI resistance, (E) charge transfer resistance, and (F) characteristic time constants as derived from fitting of impedance data with the respective equivalent circuit. Supporting Figure S12. Additional TEM-EDX mappings for the pristine material, material after 3 cycles and after 10 cycles. Na is denoted in yellow, Mn in red, Ni in green, oxygen in blue, and carbon in magenta color. Supporting Figure S13. Ex situ capillary XRD pattern of the pristine material, cathode composite after 3 and after 10 cycles. Supporting Figure S14. TEM images of active material particles at different cycling stages showing the formation of crystal defects. Supporting Figure S15. SEM cross section after direct discharge to 1.5 V (PDF)

https://doi.org/10.1021/acs.chemmater.3c01499
Chem. Mater. 2023, 35, 8065−8080

AUTHOR INFORMATION

Corresponding Authors

Lukas Fridolin Pfeiffer − *ZSW Center for Solar Energy and Hydrogen Research Baden-Württemberg, 89081 Ulm, Germany;* orcid.org/0000-0002-7473-7326; Email: Lukas.pfeiffer@zsw-bw.de

Peter Axmann − *ZSW Center for Solar Energy and Hydrogen Research Baden-Württemberg, 89081 Ulm, Germany;* Email: Peter.axmann@zsw-bw.de

Authors

Yueliang Li − *Electron Microscopy Group of Materials Science, Ulm University, 89081 Ulm, Germany*

Manuel Mundszinger − *Electron Microscopy Group of Materials Science, Ulm University, 89081 Ulm, Germany*

Jonas Geisler − *Institute of Chemistry, Humboldt-Universität zu Berlin, 12489 Berlin, Germany;* orcid.org/0009-0001-1665-3415

Claudia Pfeifer − *ZSW Center for Solar Energy and Hydrogen Research Baden-Württemberg, 89081 Ulm, Germany*

Daria Mikhailova − *Leibniz Institute for Solid State and Materials Research (IFW) Dresden e.V., 01069 Dresden, Germany;* orcid.org/0000-0002-8197-1807

Ahmad Omar − *Leibniz Institute for Solid State and Materials Research (IFW) Dresden e.V., 01069 Dresden, Germany*

Volodymyr Baran − *Deutsches Elektronen-Synchrotron (DESY), D-22607 Hamburg, Germany;* orcid.org/0000-0003-2379-3632

Johannes Biskupek − *Electron Microscopy Group of Materials Science, Ulm University, 89081 Ulm, Germany*

Ute Kaiser − *Electron Microscopy Group of Materials Science, Ulm University, 89081 Ulm, Germany*

Philipp Adelhelm − *Institute of Chemistry, Humboldt-Universität zu Berlin, 12489 Berlin, Germany;* orcid.org/0000-0003-2439-8802

Margret Wohlfahrt-Mehrens − *ZSW Center for Solar Energy and Hydrogen Research Baden-Württemberg, 89081 Ulm, Germany*

Stefano Passerini − *Helmholtz Institute Ulm, Karlsruhe Institute of Technology, 89081 Ulm, Germany; Chemistry Department, Sapienza University of Rome, 00185 Rome, Italy;* orcid.org/0000-0002-6606-5304

Complete contact information is available at: https://pubs.acs.org/10.1021/acs.chemmater.3c01499

Author Contributions

The manuscript was written through contributions of all authors. All authors have given approval to the final version of the manuscript.

Funding

This work was funded by the German Federal Ministry of Education and Research (BMBF) in the projects TRANSITION (03XP0186C), Transition Transfer (03XP0533A) and ExcellBattMat (03XP0257A, 03XP0257C and 03XP0254D) and by German Research Foundation (DFG) in the project POLIS Cluster of Excellence (ProjectID 390874152). SP acknowledges the basic funding of the Helmholtz Association.

Notes

The authors declare no competing financial interest.

ACKNOWLEDGMENTS

L.F.P., C.P., M.W.-M., and P.A. would like to thank Gisela Arnold and Bianca Anglet for ICP-OES measurements and all team members at ZSW for fruitful discussions. L.F.P. thanks Dr. Rares Scurtu (ZSW) for fruitful discussions on impedance measurements and evaluation.

ABBREVIATIONS

CEI, cathode solid electrolyte interface; EDX, energy-dispersive X-ray spectroscopy; DEMS, differential electrochemical mass spectroscopy; FFT, fast Fourier transformation; GITT, galvanostatic intermittent titration technic; HRTEM, high-resolution transmission electron microscopy; ICP-OES, inductively coupled plasma optical emission spectroscopy; LIB, lithium-ion battery; PEIS, potentiostatic electrochemical impedance spectroscopy; SEM, scanning electron microscopy; SIB, sodium-ion battery; SOC, state of charge; TEM, transmission electron microscopy; XRD, X-ray powder diffraction

REFERENCES

(1) Armand, M.; Axmann, P.; Bresser, D.; Copley, M.; Edström, K.; Ekberg, C.; Guyomard, D.; Lestriez, B.; Novák, P.; Petranikova, M.; Porcher, W.; Trabesinger, S.; Wohlfahrt-Mehrens, M.; Zhang, H. Lithium-ion batteries − Current state of the art and anticipated developments. *J. Power Sources* **2020**, *479*, No. 228708.

(2) Gür, T. M. Review of electrical energy storage technologies, materials and systems: challenges and prospects for large-scale grid storage. *Energy Environ. Sci.* **2018**, *11*, 2696−2767.

(3) Dunn, B.; Kamath, H.; Tarascon, J.-M. Electrical energy storage for the grid: a battery of choices. *Science* **2011**, *334*, 928−935.

(4) International Energy Agency. *The Role of Critical Minerals in Clean Energy Transitions:World Energy Outlook Special Report*. https://www.iea.org/reports/the-role-of-critical-minerals-in-clean-energy-transitions (accessed March 26,v2022).

(5) Boer, L.; Pescatori, A.; Stuermer, M. Energy Transition Metals. *SSRN Electron. J.***2021** DOI: 10.2139/ssrn.3945524.

(6) Kowalski, P.; Legendre, C. Raw materials critical for the green transition. *OECD Trade Policy Papers* **2023**, No. 93.

(7) Sun, Y.-K. Direction for Commercialization of O3-Type Layered Cathodes for Sodium-Ion Batteries. *ACS Energy Lett.* **2020**, *5*, 1278−1280.

(8) Tapia-Ruiz, N.; Robert Armstrong, A.; Alptekin, H.; Amores, M. A.; Au, H.; Barker, J.; Boston, R.; Brant, W. R.; Brittain, J. M.; Chen, Y.; Chhowalla, M.; Choi, Y.-S.; Costa, S. I. R.; Crespo Ribadeneyra, M.; Cussen, S. A.; Cussen, E. J.; David, W. I. F.; Desai, A. V.; Dickson, S. A. M.; Eweka, E. I.; Forero-Saboya, J. D.; Grey, C. P.; Griffin, J. M.; Gross, P.; Hua, X.; Irvine, J. T. S.; Johansson, P.; Jones, M. O.; Karlsmo, M.; Kendrick, E.; Kim, E.; Kolosov, O. V.; Li, Z.; Mertens, S. F. L.; Mogensen, R.; Monconduit, L.; Morris, R. E.; Naylor, A. J.; Nikman, S.; O'Keefe, C. A.; Ould, D. M. C.; Palgrave, R. G.; Poizot, P.; Ponrouch, A.; Renault, S.; Reynolds, E. M.; Rudola, A.; Sayers, R.; Scanlon, D. O.; Sen, S.; Seymour, V. R.; Silván, B.; Sougrati, M. T.; Stievano, L.; Stone, G. S.; Thomas, C. I.; Titirici, M.-M.; Tong, J.; Wood, T. J.; Wright, D. S.; Younesi, R. 2021 roadmap for sodium-ion batteries. *J. Phys. Energy* **2021**, *3*, No. 031503.

(9) Hasa, I.; Mariyappan, S.; Saurel, D.; Adelhelm, P.; Koposov, A. Y.; Masquelier, C.; Croguennec, L.; Casas-Cabanas, M. Challenges of today for Na-based batteries of the future: From materials to cell metrics. *J. Power Sources* **2021**, *482*, No. 228872.

(10) Rudola, A.; Rennie, A. J. R.; Heap, R.; Meysami, S. S.; Lowbridge, A.; Mazzali, F.; Sayers, R.; Wright, C. J.; Barker, J. Commercialisation of high energy density sodium-ion batteries: Faradion's journey and outlook. *J. Mater. Chem. A* **2021**, *9*, 8279−8302.

(11) Bauer, A.; Song, J.; Vail, S.; Pan, W.; Barker, J.; Lu, Y. The Scale-up and Commercialization of Nonaqueous Na-Ion Battery Technologies. *Adv. Energy Mater.* **2018**, *8*, No. 1702869.
(12) Xie, F.; Xu, Z.; Guo, Z.; Titirici, M.-M. Hard carbons for sodium-ion batteries and beyond. *Prog. Energy* **2020**, *2*, No. 042002.
(13) Moon, H.; Zarrabeitia, M.; Frank, E.; Böse, O.; Enterría, M.; Saurel, D.; Hasa, I.; Passerini, S. Assessing the Reactivity of Hard Carbon Anodes: Linking Material Properties with Electrochemical Response Upon Sodium- and Lithium-Ion Storage. *Batteries Supercaps* **2021**, *4*, 960−977.
(14) Moon, H.; Innocenti, A.; Liu, H.; Zhang, H.; Weil, M.; Zarrabeitia, M.; Passerini, S. Bio-Waste-Derived Hard Carbon Anodes Through a Sustainable and Cost-Effective Synthesis Process for Sodium-Ion Batteries. *ChemSusChem* **2023**, *16*, No. e202201713. Published Online: Nov. 11, 2022.
(15) Tarascon, J.-M. Na-ion versus Li-ion Batteries: Complementarity Rather than Competitiveness. *Joule* **2020**, *4*, 1616−1620.
(16) Larcher, D.; Tarascon, J.-M. Towards greener and more sustainable batteries for electrical energy storage. *Nat. Chem.* **2015**, *7*, 19−29.
(17) Vaalma, C.; Buchholz, D.; Weil, M.; Passerini, S. A cost and resource analysis of sodium-ion batteries. *Nat. Rev. Mater.* **2018**, *3*, No. 18013.
(18) Rudola, A.; Wright, C. J.; Barker, J. Reviewing the Safe Shipping of Lithium-Ion and Sodium-Ion Cells: A Materials Chemistry Perspective. *Energy Mater Adv* **2021**, *2021*, 37.
(19) Kuze, S.; Kageura, J.-i.; Matsumoto, S.; Nakayama, T.; Makidera, M.; Saka, M.; Yamaguchi, T.; Yamamoto, T.; Nakane, K. *Development of a Sodium Ion Secondary Battery:R&D Report*, 2013.
(20) Zhou, Q.; Li, Y.; Tang, F.; Li, K.; Rong, X.; Lu, Y.; Chen, L.; Hu, Y.-S. Thermal Stability of High Power 26650-Type Cylindrical Na-Ion Batteries. *Chin. Phys. Lett.* **2021**, *38*, No. 076501.
(21) Zuo, W.; Innocenti, A.; Zarrabeitia, M.; Bresser, D.; Yang, Y.; Passerini, S. Layered Oxide Cathodes for Sodium-Ion Batteries: Storage Mechanism, Electrochemistry, and Techno-economics. *Acc. Chem. Res.* **2023**, *56*, 284−296. Published Online: Jan. 25, 2023.
(22) Peters, J. F.; Baumann, M.; Binder, J. R.; Weil, M. On the environmental competitiveness of sodium-ion batteries under a full life cycle perspective − a cell-chemistry specific modelling approach. *Sustainable Energy Fuels* **2021**, *5*, 6414−6429.
(23) Jasper, F. B.; Späthe, J.; Baumann, M.; Peters, J. F.; Ruhland, J.; Weil, M. Life cycle assessment (LCA) of a battery home storage system based on primary data. *J. Cleaner Prod.* **2022**, *366*, No. 132899.
(24) Peters, J.; Baumann, M.; Weil, M.; Passerini, S. On the Environmental Competitiveness of Sodium-Ion Batteries − Current State of the Art in Life Cycle Assessment. In *Sodium-Ion Batteries*; Titirici, M.-M.; Adelhelm, P.; Hu, Y.-S., Eds.; Wiley, 2022; pp 551−571.
(25) Peters, J.; Peña Cruz, A.; Weil, M. Exploring the Economic Potential of Sodium-Ion Batteries. *Batteries* **2019**, *5*, 10.
(26) Ortiz-Vitoriano, Nagore.; Drewett, Nicholas E.; Gonzalo, Elena.; Rojo, Teófilo. High performance manganese-based layered oxide cathodes: overcoming the challenges of sodium ion batteries. *Energy Environ. Sci.* **2017**, *10*, 1051−1074.
(27) Goikolea, E.; Palomares, V.; Wang, S.; Larramendi, I. R. d.; Guo, X.; Wang, G.; Rojo, T. Na-Ion Batteries—Approaching Old and New Challenges. *Adv. Energy Mater.* **2020**, *10*, No. 2002055.
(28) Gonzalo, E.; Zarrabeitia, M.; Drewett, N. E.; López del Amo, J. M.; Rojo, T. Sodium manganese-rich layered oxides: Potential candidates as positive electrode for Sodium-ion batteries. *Energy Storage Mater.* **2021**, *34*, 682−707.
(29) Delmas, C.; Fouassier, C.; Hagenmuller, P. Structural classification and properties of the layered oxides. *Phys. B+C* **1980**, *99*, 81−85.
(30) Delmas, C.; Carlier, D.; Guignard, M. The Layered Oxides in Lithium and Sodium-Ion Batteries: A Solid-State Chemistry Approach. *Adv. Energy Mater.* **2021**, *11*, No. 2001201.
(31) Gupta, P.; Pushpakanth, S.; Haider, M. A.; Basu, S. Understanding the Design of Cathode Materials for Na-Ion Batteries. *ACS Omega* **2022**, *7*, 5605−5614.
(32) Paulsen, J. M.; Dahn, J. R. Studies of the layered manganese bronzes, Na2/3[Mn1−xMx]O2 with M=Co, Ni, Li, and Li2/3[Mn1−xMx]O2 prepared by ion-exchange. *Solid State Ionics* **1999**, *126*, 3−24.
(33) Lu, Z.; Dahn, J. R. In Situ X-Ray Diffraction Study of P2-Na[sub 2/3][Ni[sub 1/3]Mn[sub 2/3]]O[sub 2]. *J. Electrochem. Soc.* **2001**, *148*, A1225.
(34) Lu, Z.; Dahn, J. R. Intercalation of Water in P2, T2 and O2 Structure A z [Co x Ni 1/3-x Mn 2/3]O 2. *Chem. Mater.* **2001**, *13*, 1252−1257.
(35) Lee, D. H.; Xu, J.; Meng, Y. S. An advanced cathode for Na-ion batteries with high rate and excellent structural stability. *Phys. Chem. Chem. Phys.* **2013**, *15*, 3304−3312. Published Online: Jan. 29, 2013
(36) Kubota, K.; Komaba, S. Review—Practical Issues and Future Perspective for Na-Ion Batteries. *J. Electrochem. Soc.* **2015**, *162*, A2538−A2550.
(37) Yoshida, H.; Yabuuchi, N.; Kubota, K.; Ikeuchi, I.; Garsuch, A.; Schulz-Dobrick, M.; Komaba, S. P2-type Na(2/3)Ni(1/3)Mn(2/3-x)Ti(x)O2 as a new positive electrode for higher energy Na-ion batteries. *Chem. Commun.* **2014**, *50*, 3677−3680.
(38) Risthaus, T.; Zhou, D.; Cao, X.; He, X.; Qiu, B.; Wang, J.; Zhang, L.; Liu, Z.; Paillard, E.; Schumacher, G.; Winter, M.; Li, J. A high-capacity P2 Na2/3Ni1/3Mn2/3O2 cathode material for sodium ion batteries with oxygen activity. *J. Power Sources* **2018**, *395*, 16−24.
(39) Mao, J.; Liu, X.; Liu, J.; Jiang, H.; Zhang, T.; Shao, G.; Ai, G.; Mao, W.; Feng, Y.; Yang, W.; Liu, G.; Dai, K. P2-type Na 2/3 Ni 1/3 Mn 2/3 O 2 Cathode Material with Excellent Rate and Cycling Performance for Sodium-Ion Batteries. *J. Electrochem. Soc.* **2019**, *166*, A3980−A3986.
(40) Gutierrez, A.; Dose, W. M.; Borkiewicz, O.; Guo, F.; Avdeev, M.; Kim, S.; Fister, T. T.; Ren, Y.; Bareño, J.; Johnson, C. S. On Disrupting the Na + -Ion/Vacancy Ordering in P2-Type Sodium−Manganese−Nickel Oxide Cathodes for Na + -Ion Batteries. *J. Phys. Chem. C* **2018**, *122*, 23251−23260.
(41) Manikandan, P.; Ramasubramonian, D.; Shaijumon, M. M. Layered P2-type Na0.5Ni0.25Mn0.75O2 as a high performance cathode material for sodium-ion batteries. *Electrochim. Acta* **2016**, *206*, 199−206.
(42) Pfeiffer, L. F.; Jobst, N.; Gauckler, C.; Lindén, M.; Marinaro, M.; Passerini, S.; Wohlfahrt-Mehrens, M.; Axmann, P. Layered P2-NaxMn3/4Ni1/4O2 Cathode Materials For Sodium-Ion Batteries: Synthesis, Electrochemistry and Influence of Ambient Storage. *Front. Energy Res.* **2022**, *10*, 305.
(43) Dai, K.; Mao, J.; Zhuo, Z.; Feng, Y.; Mao, W.; Ai, G.; Pan, F.; Chuang, Y.-d.; Liu, G.; Yang, W. Negligible voltage hysteresis with strong anionic redox in conventional battery electrode. *Nano Energy* **2020**, *74*, No. 104831.
(44) Zhang, Y.; Wu, M.; Ma, J.; Wei, G.; Ling, Y.; Zhang, R.; Huang, Y. Revisiting the Na2/3Ni1/3Mn2/3O2 Cathode: Oxygen Redox Chemistry and Oxygen Release Suppression. *ACS Cent. Sci.* **2020**, *6*, 232−240. Published Online: Jan. 29, 2020.
(45) Zhang, J.; Wang, W.; Wang, W.; Wang, S.; Li, B. Comprehensive Review of P2-Type Na2/3Ni1/3Mn2/3O2, a Potential Cathode for Practical Application of Na-Ion Batteries. *ACS Appl. Mater. Interfaces* **2019**, *11*, 22051−22066. Published Online: Jun. 11, 2019.
(46) Alvarado, J.; Ma, C.; Wang, S.; Nguyen, K.; Kodur, M.; Meng, Y. S. Improvement of the Cathode Electrolyte Interphase on P2-Na2/3Ni1/3Mn2/3O2 by Atomic Layer Deposition. *ACS Appl. Mater. Interfaces* **2017**, *9*, 26518−26530. Published Online: Jul. 27, 2017.
(47) Liu, Y.; Fang, X.; Zhang, A.; Shen, C.; Liu, Q.; Enaya, H. A.; Zhou, C. Layered P2-Na2/3[Ni1/3Mn2/3]O2 as high-voltage cathode for sodium-ion batteries: The capacity decay mechanism and Al2O3 surface modification. *Nano Energy* **2016**, *27*, 27−34.

https://doi.org/10.1021/acs.chemmater.3c01499
Chem. Mater. 2023, 35, 8065−8080

(48) Momma, K.; Izumi, F. VESTA 3 for three-dimensional visualization of crystal, volumetric and morphology data. *J. Appl. Crystallogr.* **2011**, *44*, 1272−1276.
(49) Zuo, W.; Qiu, J.; Liu, X.; Ren, F.; Liu, H.; He, H.; Luo, C.; Li, J.; Ortiz, G. F.; Duan, H.; Liu, J.; Wang, M.-S.; Li, Y.; Fu, R.; Yang, Y. The stability of P2-layered sodium transition metal oxides in ambient atmospheres. *Nat. Commun.* **2020**, *11*, No. 3544. Published Online: Jul. 15, 2020.
(50) Dippel, A.-C.; Liermann, H.-P.; Delitz, J. T.; Walter, P.; Schulte-Schrepping, H.; Seeck, O. H.; Franz, H. Beamline P02.1 at PETRA III for high-resolution and high-energy powder diffraction. *J. Synchrotron Radiat.* **2015**, *22*, 675−687. Published Online: Apr. 14, 2015
(51) Herklotz, M.; Weiß, J.; Ahrens, E.; Yavuz, M.; Mereacre, L.; Kiziltas-Yavuz, N.; Dräger, C.; Ehrenberg, H.; Eckert, J.; Fauth, F.; Giebeler, L.; Knapp, M. A novel high-throughput setup for in situ powder diffraction on coin cell batteries. *J. Appl. Crystallogr.* **2016**, *49*, 340−345.
(52) Zuo, W.; Xiao, Z.; Zarrabeitia, M.; Xue, X.; Yang, Y.; Passerini, S. Guidelines for Air-Stable Lithium/Sodium Layered Oxide Cathodes. *ACS Mater. Lett.* **2022**, *4*, 1074−1086.
(53) Ectors, D.; Goetz-Neunhoeffer, F.; Neubauer, J. A generalized geometric approach to anisotropic peak broadening due to domain morphology. *J. Appl. Crystallogr.* **2015**, *48*, 189−194.
(54) Ectors, D.; Goetz-Neunhoeffer, F.; Neubauer, J. Domain size anisotropy in the double-Voigt approach: an extended model. *J. Appl. Crystallogr.* **2015**, *48*, 1998−2001.
(55) Ectors, D.; Goetz-Neunhoeffer, F.; Neubauer, J. Routine (an)isotropic crystallite size analysis in the double-Voigt approximation done right? *Powder Diffr.* **2017**, *32*, S27−S34.
(56) Parant, J.-P.; Olazcuaga, R.; Devalette, M.; Fouassier, C.; Hagenmuller, P. Sur quelques nouvelles phases de formule NaxMnO2 (x ⩽ 1). *J. Solid State Chem.* **1971**, *3*, 1−11.
(57) Gauckler, C.; Dillenz, M.; Maroni, F.; Pfeiffer, L. F.; Biskupek, J.; Sotoudeh, M.; Fu, Q.; Kaiser, U.; Dsoke, S.; Euchner, H.; Axmann, P.; Wohlfahrt-Mehrens, M.; Groß, A.; Marinaro, M. Detailed Structural and Electrochemical Comparison between High Potential Layered P2-NaMnNi and Doped P2-NaMnNiMg Oxides. *ACS Appl. Energy Mater.* **2022**, *5*, 13735−13750.
(58) Bredar, A. R. C.; Chown, A. L.; Burton, A. R.; Farnum, B. H. Electrochemical Impedance Spectroscopy of Metal Oxide Electrodes for Energy Applications. *ACS Appl. Energy Mater.* **2020**, *3*, 66−98.
(59) Lazanas, A. C.; Prodromidis, M. I. Electrochemical Impedance Spectroscopy-A Tutorial. *ACS Meas. Sci. Au* **2023**, *3*, 162−193. Published Online: March 8, 2023.
(60) Bard, A. J.; Faulkner, L. R. *Electrochemical Methods: Fundamentals and Applications*, 2nd ed.; Wiley, 2001.
(61) Muñoz-Márquez, M. Á; Zarrabeitia, M.; Passerini, S.; Rojo, T. Structure, Composition, Transport Properties, and Electrochemical Performance of the Electrode-Electrolyte Interphase in Non-Aqueous Na-Ion Batteries. *Adv. Mater. Interfaces* **2022**, *9*, No. 2101773.
(62) Brug, G. J.; van den Eeden, A.L.G.; Sluyters-Rehbach, M.; Sluyters, J. H. The analysis of electrode impedances complicated by the presence of a constant phase element. *J. Electroanal. Chem. Interfacial Electrochem.* **1984**, *176*, 275−295.
(63) Bisquert, J.; Garcia-Belmonte, G.; Bueno, P.; Longo, E.; Bulhões, L.O.S. Impedance of constant phase element (CPE)-blocked diffusion in film electrodes. *J. Electroanal. Chem.* **1998**, *452*, 229−234.
(64) Orazem, M. E.; Shukla, P.; Membrino, M. A. Extension of the measurement model approach for deconvolution of underlying distributions for impedance measurements. *Electrochim. Acta* **2002**, *47*, 2027−2034.
(65) Rammelt, U.; Reinhard, G. On the applicability of a constant phase element (CPE) to the estimation of roughness of solid metal electrodes. *Electrochim. Acta* **1990**, *35*, 1045−1049.
(66) Hirschorn, B.; Orazem, M. E.; Tribollet, B.; Vivier, V.; Frateur, I.; Musiani, M. Determination of effective capacitance and film thickness from constant-phase-element parameters. *Electrochim. Acta* **2010**, *55*, 6218−6227.
(67) Lasia, A. Electrochemical Impedance Spectroscopy and its Applications. In *Modern Aspects of Electrochemistry*; Conway, B. E.; Bockris, J. O.'M.; White, R. E., Eds.; Modern Aspects of Electrochemistry; Kluwer Academic Publishers, 2002; pp 143−248.
(68) Carbonari, G.; Müller, V.; Scurtu, R.-G.; Memm, M.; Hoffmann, A.; Wohlfahrt-Mehrens, M. Communication—Edge Quality Contribution on the Electrical Impedance of Lithium-Ion Batteries Electrodes. *J. Electrochem. Soc.* **2020**, *167*, No. 080504.
(69) Pritzl, D.; Bumberger, A. E.; Wetjen, M.; Landesfeind, J.; Solchenbach, S.; Gasteiger, H. A. Identifying Contact Resistances in High-Voltage Cathodes by Impedance Spectroscopy. *J. Electrochem. Soc.* **2019**, *166*, A582−A590.
(70) Chen, X.; Li, L.; Liu, M.; Huang, T.; Yu, A. Detection of lithium plating in lithium-ion batteries by distribution of relaxation times. *J. Power Sources* **2021**, *496*, No. 229867.
(71) Hahn, M.; Schindler, S.; Triebs, L.-C.; Danzer, M. A. Optimized Process Parameters for a Reproducible Distribution of Relaxation Times Analysis of Electrochemical Systems. *Batteries* **2019**, *5*, 43.
(72) Shafiei Sabet, P.; Sauer, D. U. Separation of predominant processes in electrochemical impedance spectra of lithium-ion batteries with nickel-manganese-cobalt cathodes. *J. Power Sources* **2019**, *425*, 121−129.
(73) Shafiei Sabet, P.; Warnecke, A. J.; Meier, F.; Witzenhausen, H.; Martinez-Laserna, E.; Sauer, D. U. Non-invasive yet separate investigation of anode/cathode degradation of lithium-ion batteries (nickel−cobalt−manganese vs. graphite) due to accelerated aging. *J. Power Sources* **2020**, *449*, No. 227369.
(74) Oswald, S.; Pritzl, D.; Wetjen, M.; Gasteiger, H. A. Novel Method for Monitoring the Electrochemical Capacitance by In Situ Impedance Spectroscopy as Indicator for Particle Cracking of Nickel-Rich NCMs: Part I. Theory and Validation. *J. Electrochem. Soc.* **2020**, *167*, No. 100511.
(75) Nellist, P. D.; Pennycook, S. J. The principles and interpretation of annular dark-field Z-contrast imaging. In *Advances in Imaging and Electron Physics*; Elsevier, 2000; pp 147−203.
(76) Jung, R.; Metzger, M.; Maglia, F.; Stinner, C.; Gasteiger, H. A. Chemical versus Electrochemical Electrolyte Oxidation on NMC111, NMC622, NMC811, LNMO, and Conductive Carbon. *J. Phys. Chem. Lett.* **2017**, *8*, 4820−4825. Published Online: Sep. 21, 2017.
(77) Jung, R.; Metzger, M.; Maglia, F.; Stinner, C.; Gasteiger, H. A. Oxygen Release and Its Effect on the Cycling Stability of LiNi x Mn y Co z O 2 (NMC) Cathode Materials for Li-Ion Batteries. *J. Electrochem. Soc.* **2017**, *164*, A1361−A1377.
(78) Jung, R.; Strobl, P.; Maglia, F.; Stinner, C.; Gasteiger, H. A. Temperature Dependence of Oxygen Release from LiNi 0.6 Mn 0.2 Co 0.2 O 2 (NMC622) Cathode Materials for Li-Ion Batteries. *J. Electrochem. Soc.* **2018**, *165*, A2869−A2879.
(79) Lin, F.; Markus, I. M.; Nordlund, D.; Weng, T.-C.; Asta, M. D.; Xin, H. L.; Doeff, M. M. Surface reconstruction and chemical evolution of stoichiometric layered cathode materials for lithium-ion batteries. *Nat. Commun.* **2014**, *5*, No. 3529. Published Online: March 27, 2014.
(80) Abraham, D. P.; Twesten, R. D.; Balasubramanian, M.; Petrov, I.; McBreen, J.; Amine, K. Surface changes on LiNi0.8Co0.2O2 particles during testing of high-power lithium-ion cells. *Electrochem. Commun.* **2002**, *4*, 620−625.
(81) Bianchini, M.; Roca-Ayats, M.; Hartmann, P.; Brezesinski, T.; Janek, J. There and Back Again-The Journey of LiNiO2 as a Cathode Active Material. *Angew. Chem., Int. Ed.* **2019**, *58*, 10434−10458. Published Online: May. 2, 2019.
(82) House, R. A.; Maitra, U.; Jin, L.; Lozano, J. G.; Somerville, J. W.; Rees, N. H.; Naylor, A. J.; Duda, L. C.; Massel, F.; Chadwick, A. V.; Ramos, S.; Pickup, D. M.; McNally, D. E.; Lu, X.; Schmitt, T.; Roberts, M. R.; Bruce, P. G. What Triggers Oxygen Loss in Oxygen Redox Cathode Materials? *Chem. Mater.* **2019**, *31*, 3293−3300.
(83) Wang, Q.; Mariyappan, S.; Rousse, G.; Morozov, A. V.; Porcheron, B.; Dedryvère, R.; Wu, J.; Yang, W.; Zhang, L.; Chakir, M.; Avdeev, M.; Deschamps, M.; Yu, Y.-S.; Cabana, J.; Doublet, M.-L.;

Abakumov, A. M.; Tarascon, J.-M. Unlocking anionic redox activity in O3-type sodium 3d layered oxides via Li substitution. *Nat. Mater.* **2021**, *20*, 353−361. Published Online: Jan. 11, 2021.
(84) Wandt, J.; Freiberg, A. T. S.; Ogrodnik, A.; Gasteiger, H. A. Singlet oxygen evolution from layered transition metal oxide cathode materials and its implications for lithium-ion batteries. *Mater. Today* **2018**, *21*, 825−833.
(85) Metzger, M.; Strehle, B.; Solchenbach, S.; Gasteiger, H. A. Origin of H 2 Evolution in LIBs: H 2 O Reduction vs. Electrolyte Oxidation. *J. Electrochem. Soc.* **2016**, *163*, A798−A809.
(86) Dreyer, S. L.; Kondrakov, A.; Janek, J.; Brezesinski, T. In situ analysis of gas evolution in liquid- and solid-electrolyte-based batteries with current and next-generation cathode materials. *J. Mater. Res.* **2022**, *37*, 3146−3168.
(87) Metzger, M.; Gasteiger, H. A. Diagnosing Battery Degradation via Gas Analysis. *Energy Environ. Mater.* **2022**, *5*, 688−692.
(88) Oswald, S.; Pritzl, D.; Wetjen, M.; Gasteiger, H. A. Novel Method for Monitoring the Electrochemical Capacitance by In Situ Impedance Spectroscopy as Indicator for Particle Cracking of Nickel-Rich NCMs: Part II. Effect of Oxygen Release Dependent on Particle Morphology. *J. Electrochem. Soc.* **2021**, *168*, No. 120501.
(89) Oswald, S.; Riewald, F.; Gasteiger, H. A. Novel Method for Monitoring the Electrochemical Capacitance by In Situ Impedance Spectroscopy as Indicator for Particle Cracking of Nickel-Rich NCMs: Part III. Development of a Simplified Measurement Setup. *J. Electrochem. Soc.* **2022**, *169*, No. 040552.
(90) Villars, P.; Hulliger, F. *NiO rt conductivity/resistivity: Datasheet from "PAULING FILE Multinaries Edition − 2022" in SpringerMaterials:Inorganic Solid Phases*. https://materials.springer.com/isp/physical-property/docs/ppp_f73df1ee2594a3e0e4ed3ab01a421a64 (accessed June 7th, 2023).
(91) Clément, R. J.; Lun, Z.; Ceder, G. Cation-disordered rocksalt transition metal oxides and oxyfluorides for high energy lithium-ion cathodes. *Energy Environ. Sci.* **2020**, *13*, 345−373.
(92) Yu, T.-Y.; Ryu, H.-H.; Han, G.; Sun, Y.-K. Understanding the Capacity Fading Mechanisms of O3-Type Na[Ni 0.5 Mn 0.5]O 2 Cathode for Sodium-Ion Batteries. *Adv. Energy Mater.* **2020**, *10*, No. 2001609.
(93) Paulsen, J. M.; Thomas, C. L.; Dahn, J. R. Layered Li-Mn-Oxide with the O2 Structure: A Cathode Material for Li-Ion Cells Which Does Not Convert to Spinel. *J. Electrochem. Soc.* **1999**, *146*, 3560.
(94) Yabuuchi, N.; Yano, M.; Kuze, S.; Komaba, S. Electrochemical behavior and structural change of spinel-type Li[Li Mn2−]O4 (x= 0 and 0.2) in sodium cells. *Electrochim. Acta* **2012**, *82*, 296−301.
(95) Clément, R. J.; Bruce, P. G.; Grey, C. P. Review—Manganese-Based P2-Type Transition Metal Oxides as Sodium-Ion Battery Cathode Materials. *J. Electrochem. Soc.* **2015**, *162*, A2589.
(96) Kim, S.; Ma, X.; Ong, S. P.; Ceder, G. A comparison of destabilization mechanisms of the layered Na(x)MO2 and Li(x)MO2 compounds upon alkali de-intercalation. *Phys. Chem. Chem. Phys.* **2012**, *14*, 15571−15578. Published Online: Oct. 17, 2012.
(97) Cheng, C.; Ding, M.; Yan, T.; Jiang, J.; Mao, J.; Feng, X.; Chan, T.-S.; Li, N.; Zhang, L. Anionic Redox Activities Boosted by Aluminum Doping in Layered Sodium-Ion Battery Electrode. *Small Methods* **2022**, *6*, No. e2101524. Published Online: Jan. 27, 2022.
(98) Ma, C.; Alvarado, J.; Xu, J.; Clément, R. J.; Kodur, M.; Tong, W.; Grey, C. P.; Meng, Y. S. Exploring Oxygen Activity in the High Energy P2-Type Na0.78Ni0.23Mn0.69O2 Cathode Material for Na-Ion Batteries. *J. Am. Chem. Soc.* **2017**, *139*, 4835−4845. Published Online: March 22, 2017.
(99) Rong, X.; Hu, E.; Lu, Y.; Meng, F.; Zhao, C.; Wang, X.; Zhang, Q.; Yu, X.; Gu, L.; Hu, Y.-S.; Li, H.; Huang, X.; Yang, X.-Q.; Delmas, C.; Chen, L. Anionic Redox Reaction-Induced High-Capacity and Low-Strain Cathode with Suppressed Phase Transition. *Joule* **2019**, *3*, 503−517.
(100) Somerville, J. W.; Sobkowiak, A.; Tapia-Ruiz, N.; Billaud, J.; Lozano, J. G.; House, R. A.; Gallington, L. C.; Ericsson, T.; Häggström, L.; Roberts, M. R.; Maitra, U.; Bruce, P. G. Nature of the "Z"-phase in layered Na-ion battery cathodes. *Energy Environ. Sci.* **2019**, *12*, 2223−2232.

https://doi.org/10.1021/acs.chemmater.3c01499
Chem. Mater. 2023, 35, 8065−8080